


Phase evolution of Ce-based heavy-fermion superconductors under compression: A combined first-principles and effective-model study

Hao-Tian Ma,^{1,*} Peng-Fei Tian,^{1,*} Da-Liang Guo,¹ Xing Ming,¹ Xiao-Jun Zheng ¹, Yu Liu ², and Huan Li ^{1,†}

¹College of Physics and Electronic Information Engineering, Guilin University of Technology, Guilin 541004, China

²Laboratory of Computational Physics, Institute of Applied Physics and Computational Mathematics, Beijing 100088, China



(Received 12 October 2023; revised 14 March 2024; accepted 10 May 2024; published 22 May 2024)

In many Ce-based superconductors, superconducting (SC) phases emerge or can be tuned in proximity to the antiferromagnetic (AFM) quantum critical point (QCP), but so far the explicit phase evolution near the QCP lacks theoretical understanding. Here, by combing the density functional theory plus dynamical mean-field theory (DFT+DMFT) with effective-model calculations, we provide a theoretical description for Ce-based superconductors under compression. DFT+DMFT calculations for the normal states reveal that the Kondo hybridizations are significantly enhanced under compression, while the initially localized f electrons become fully itinerant via localized-itinerant crossover. We then construct an effective model and show that with the extracted Kondo coupling and RKKY exchange strengths from first-principles calculations, the ground-state phases of these materials can be properly predicted. We also show that the coexistence of magnetic correlation and Kondo hybridization can drive AFM+SC coexisting states in a narrow compression region. Under compression, competition between Kondo and RKKY interactions can drive successive transitions, from the AFM phase to the AFM+SC coexisting phase, then to the paramagnetic SC phase via an AFM transition which generates the QCP, and finally to the normal Kondo paramagnetic (KP) phase through an SC-KP transition induced by the localized-itinerant crossover. Our paper gives proper explanation to the pressure-induced QCP and SC-KP transition and to the phase evolution in pressured Ce-based superconductors, and can help one to understand the SC states around the ferromagnetic quantum transition points in uranium-based superconductors.

DOI: [10.1103/PhysRevB.109.195164](https://doi.org/10.1103/PhysRevB.109.195164)

I. INTRODUCTION

Heavy-fermion (HF) materials are characterized by Kondo hybridization between conduction and f electrons, in which the f electrons are correlated via Coulomb repulsion and tend to form local moments. At low temperature, the Kondo screening of f electrons by conducting electrons induces a many-body Kondo singlet state, resulting in strong enhancement of quasiparticle mass and intense Kondo resonance peak in the density of states (DOS) near the Fermi level [1]. In some HF materials such as CeCu_2Si_2 , CeMIn_5 ($M=\text{Rh}$, Co , Ir), and recently discovered CeRh_2As_2 and CeSb_2 , superconducting (SC) phases have been observed with large coefficients of specific heat, illustrating the emergence of heavy-fermion superconductivity [2–10]. In these heavy-fermion SC compounds, rich phases and phase transitions are observed under pressure. At ambient pressure, CeCu_2Si_2 , CeRhIn_5 , and CeSb_2 are antiferromagnetically ordered, then they enter into SC phases when AFM orders are gradually suppressed at higher pressure, showing an arc-shaped SC critical temperature T_c surrounding the AFM quantum critical point (QCP) in their pressure-temperature phase diagrams [3–5]. In the intermediate pressure region in CeCu_2Si_2 , CeRhIn_5 and CeSb_2 , etc., AFM orders can coexist with

heavy-fermion superconductivity, evidencing the emergence of an AFM+SC coexisting phase [11–16]. By contrast, for CeRh_2As_2 , the ground state is already an AFM+SC phase at ambient pressure, and its T_c gradually decreases with enhanced pressure [17,18], while for CeCoIn_5 and CeIrIn_5 , at ambient pressure, the SC phases emerge without AFM long-range order [6,7].

The vicinity of many typical Ce-based heavy-fermion SC compounds to AFM orders establishes that magnetic correlations between f electrons play an important role in the development of superconductivity; in particular, the occurrence of superconductivity near the pressure-induced magnetic QCP in CePd_2Si_2 and CeCu_2Si_2 supports a SC pairing mediated by AFM correlations [14,19–24]. In addition, the majority of heavy-fermion SC compounds preserve space-inversion symmetry, ensuring that the Cooper pairs arise in the spin-singlet even-parity channel [25,26]. In spite of these theoretical investigations, there remains a lack of explicit theoretical explanation so far for the microscopic mechanism governing the coexistence of heavy-fermion SC with AFM order at the intermediate pressure region. In particular, the successive phase evolution with applied pressure in heavy-fermion SC materials and why they exhibit distinct ground-state phases at ambient pressure still lack deep understanding beyond the phenomenological level [27,28].

In this paper, we systematically explore the effect of pressure on typical Ce-based heavy-fermion SC materials through density functional theory combined with dynamical

*These authors contributed equally to this work.

†lihuan@glut.edu.cn

mean-field theory (DFT+DMFT), in company with effective-model description. First, by DFT+DMFT calculations for the normal states of these materials at low temperature, we show that volume compression can significantly enhance the Kondo hybridization between conduction and f electrons, meanwhile weakening the local-moment degree of f electrons, then eventually driving a localized-to-itinerant crossover of the Ce- $4f$ states at rather high volume compression ratio. Based on these DFT+DMFT results, we construct an effective Kondo-Heisenberg lattice model and successfully derive an AFM+SC coexisting phase in which the SC pairing is mediated by short-range singlet pairing between f electrons in the context of c - f hybridization and AFM long-range order. By including the pressure variation of Kondo coupling J_K and Ruderman-Kittel-Kasuya-Yosida (RKKY) superexchange strength J_H extracted via first-principles calculations, we find that in the context of competition between J_K and J_H , the increasing pressure can drive successive phase transitions, from an AFM ordered phase to AFM+SC coexisting phase, then to a paramagnetic heavy-fermion SC phase after an AFM transition, and finally to a Kondo paramagnetic (KP) phase through an SC transition, in which the AFM transition can be related to the QCP in heavy-fermion SC materials, while the SC transition is induced by localized-to-itinerant crossover. Such a phase-evolution process gives a qualitative explanation to the experimental phase diagrams of heavy-fermion SC compounds, such as CeSb₂, CeRhIn₅, and CeCu₂Si₂ under pressure [3–5]. In addition, we show that the ground-state phases of a variety of Ce-based SC compounds at ambient pressure can be predicted properly according to their degrees of RKKY and Kondo coupling strengths. Furthermore, the localized-to-itinerant crossover in CeRh₂As₂ under compression provides a theoretical predication for SC transition at higher pressure, which may be verified by future experiments. Our effective-model studies plus DFT+DMFT calculations eventually give an appropriate description for typical Ce-based heavy-fermion SC compounds, to their phases and phase evolutions under ambient and higher pressures.

The rest of this paper is arranged as follows: In Sec. II, we perform DFT+DMFT simulations of typical Ce-based superconductors under compression. Through synthetical analyses of the self-energy, impurity hybridization function, DOS, momentum-resolved spectral function, and spin susceptibility, we will estimate the strength of Kondo hybridization and degree of f localization at ambient pressure and examine their variation tendency with pressure, through which we identify the localized-to-itinerant crossover at certain compression percentage. In Sec. III, we construct a minimal effective model, and perform mean-field calculation to derive the AFM+SC coexisting phase. Then, by combining the DFT+DMFT and DFT+ U results of Kondo coupling and RKKY strengths with the effective model, we give predictions of Ce-based superconductors for their ground-state phases and phase evolutions from ambient pressure. Eventually, our results by combining first-principles simulations with model calculations successfully depict a qualitative phase diagram of heavy-fermion SC compounds under ambient and increasing pressure. Section IV will give a brief conclusion and discussion.

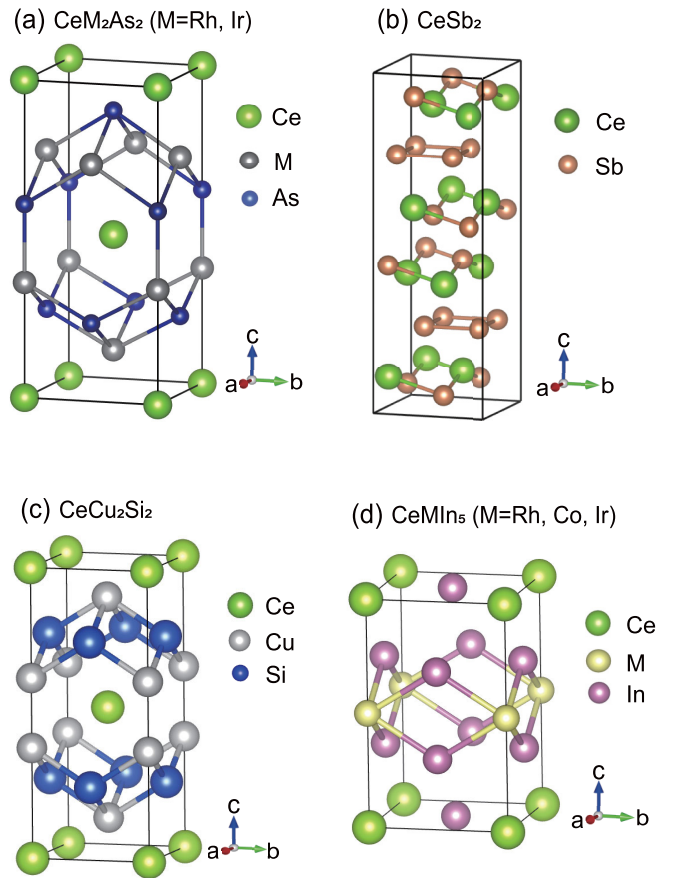


FIG. 1. Lattice structures of Ce-based superconductors. These compounds are all crystalized with global inversion symmetry. In (a), the local centrosymmetries of Ce sites in CeRh₂As₂ and CeIr₂As₂ with tetragonal CaBa₂Ge₂-type structure are broken [30]. On the ab plane, the Ce atoms in (a), (c), and (d) form a square-lattice structure.

II. DFT+DMFT SIMULATIONS AND LOCALIZED-ITINERANT CROSSOVER

We adopt the DFT+DMFT method built up in the EDMFT code package [29] to explore the pressure effect in recently discovery heavy-fermion SC compounds CeRh₂As₂ and CeSb₂ [5,8], of which the lattice structures are shown in Fig. 1. In DFT+DMFT simulation, the DFT part is implemented by full-potential linear augmented plane-wave method embodied in the WIEN2K package, and the generated single-particle Kohn-Sham Hamiltonian \hat{H}_{KS} is combined with an interacting term \hat{H}_{int} which includes on-site Coulomb repulsion U and Hund's coupling J on Ce- $4f$ electrons, together with a double-counting term Σ_{dc} for self-energy, then the constructed lattice model $\hat{H}_{DFT+DMFT} = \hat{H}_{KS} + \hat{H}_{int} - \Sigma_{dc}$ is solved within the single-site DMFT algorithm, in which the states within $[-10, 10]$ eV from the Fermi level are projected into the Anderson impurity problems. We use nominal double-counting $\Sigma_{dc} = U(n_f - 1/2) - J/2(n_f - 1)$, and continuous-time quantum Monte Carlo method (CTQMC) as the impurity solver. To obtain real-frequency self-energy, we use the maximum-entropy method to perform analytical continuation of the output imaginary-frequency self-energy. In the DFT part, we use around 2000 k points in the Brillouin

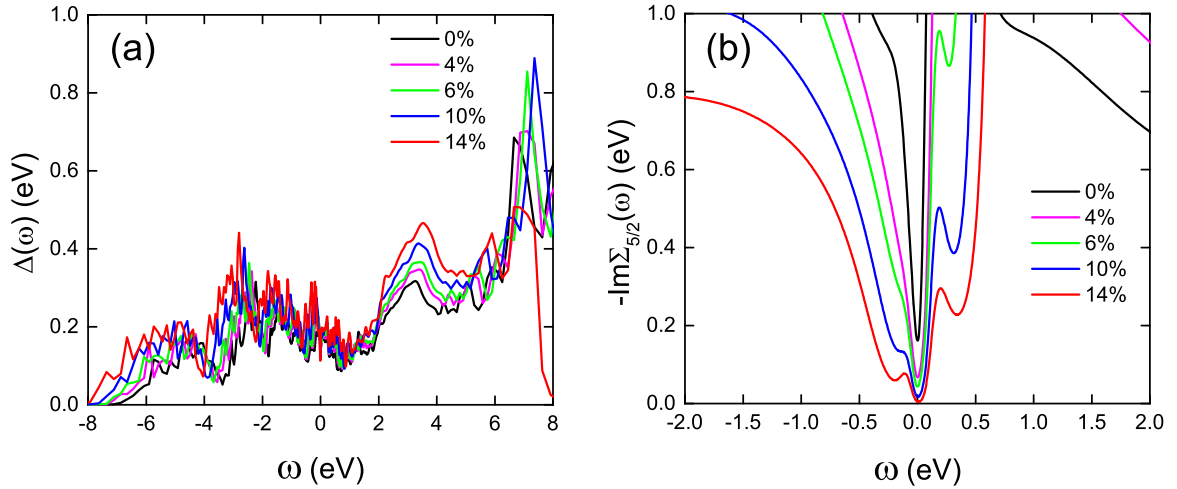


FIG. 2. (a) Hybridization function $\Delta(\omega)$ and (b) imaginary part of real-frequency self-energy $-\text{Im}\Sigma_{5/2}(\omega)$ of CeRh_2As_2 at various compression ratios, all at temperature $T = 20$ K. Upon increase of compression ratio, the zero-frequency self-energy $-\text{Im}\Sigma_{5/2}(0)$ is greatly reduced, while the hybridization function is enhanced in wide energy range.

zone integration ($16 \times 16 \times 7$ and $20 \times 20 \times 4$ \mathbf{k} -mesh for CeRh_2As_2 and CeSb_2 , respectively), and spin-orbital coupling (SOC) is included throughout the calculations. For CeRh_2As_2 and CeSb_2 , a typical value of $U = 5.5$ eV and $J = 0.7$ eV are used for Ce- $4f$ orbitals [31,32]. In each CTQMC calculation, we use 128 CPU cores to run $(3 \sim 10) \times 10^8$ QMC steps, from temperature 800 K to 20 K. The DFT+DMFT simulations are performed iteratively to reach full-charge self-consistency within 50 iterations, then an additional five iterations are executed to average the outputs to reduce numerical noise.

First, we discuss CeRh_2As_2 . Figure 2(a) shows the hybridization function $\Delta(\omega)$ on the real-frequency axis at 20 K, which is related to the imaginary part of impurity hybridization function $\tilde{\Delta}(\omega)$ by $\Delta(\omega) = -\frac{1}{\pi}\text{Im}\tilde{\Delta}(\omega)$. It can be seen that as the compression rate increases, the hybridization function exhibits significant enhancement in a wide energy range, indicating that the c - f Kondo hybridization strength also increases accordingly. As shown in Fig. 2(b), at 20 K, the imaginary part of Ce- $4f_{5/2}$ self-energy $-\text{Im}\Sigma_{5/2}(\omega)$ exhibits an evident dip structure around zero frequency, which induces a sharp Kondo resonance peak near the Fermi level at low temperature, as shown in Figs. 3(a) and 3(b), in which the additional peaks around 0.36 eV above E_F are contributed by $4f_{7/2}$ state. As the compression rate increases, the zero-frequency magnitude of $-\text{Im}\Sigma_{5/2}(\omega)$ decreases rapidly (reaches 5.2 meV at 14% volume compression), leading to significant enhancement of Kondo resonance peak, as illustrated in Fig. 3(c). Above 6% compression rate, Ce- $4f_{5/2}$ self-energy can be well fitted by a parabolic function near zero frequency as $-\text{Im}\Sigma_{5/2}(\omega) \approx \alpha(\omega - \omega_0)^2 + \Sigma_0$ with very small ω_0 and Σ_0 , signaling the appearance of heavy Fermi liquid behavior as a result of enhanced Kondo hybridization under compression [30]. The appearance of Kondo resonance can be witnessed via momentum-resolved spectral function $A(\mathbf{k}, \omega)$, which can be related directly to ARPES measurements. Figure 4(a) illustrates $A(\mathbf{k}, \omega)$ between $[-3, 5]$ eV, in which the broad lower and upper Hubbard bands appear

around -2 and 3 eV, respectively, and roughly correspond to $\pm U/2$. From Fig. 4(b), the spectral weight of the lower Hubbard band is quite weak, while the weight of the upper Hubbard band is rather intense, in accord with the characteristics of many Ce-based materials. Figure 5 shows $A(\mathbf{k}, \omega)$ of CeRh_2As_2 at volume-compression ratios from 0%, and 4% to 10%. The hybridization of conduction electrons with $4f_{5/2}$ or $4f_{7/2}$ states gives rise to two groups of flat heavy-fermion bands near the Fermi level (set as 0 eV) and 0.36 eV above, respectively. Since c - f hybridization is enhanced with increasing compression, the spectral weight of these heavy-fermion bands becomes gradually intense and are eventually clearly resolved at 10% compression rate; see the enlarged view in Fig. 5(i). In addition, the nonsymmorphic symmetries in the space group of CeRh_2As_2 ($P4/nmm$, No. 129) preserve Dirac-type band crossings along X-R and M-A paths in the Brillouin zone, which can be clear seen in Fig. 5(i). Therefore, under compression, CeRh_2As_2 can be classified as a heavy node-line Dirac semimetal, similar to the case of CePt_2Si_2 [30].

The formation of sharply resolved heavy-fermion bands at 10% volume compression [Fig. 5(i)] indicates that now the local moments are well screened by conduction electrons and Ce- $4f$ electrons become fully itinerant, i.e., a localized-itinerant crossover takes place [33], leading to a heavy Fermi liquid state. To evaluate the compression rate and temperature at which the localized-itinerant crossover occurs, we calculate the local spin susceptibility χ_s of Ce- $4f$ states during DFT+DMFT iterations, and the results are displayed in Fig. 6. Figures 6(a) and 6(b) show the temperature dependence of χ_s and its inverse χ_s^{-1} , respectively, at five different compression rates ranging from 0% to 14%, in which the solid lines denote the fitted Curis-Weiss functions $\chi_s = C/(T + \theta)$. The coincidence of χ_s dots with Curis-Weiss line at 0% compression confirms the local-moment nature of CeRh_2As_2 at ambient pressure. At low compression rate (4%), the susceptibility only slightly diverges from Curis-Weiss line at low temperature, while above 6% compression rate, a local maximum

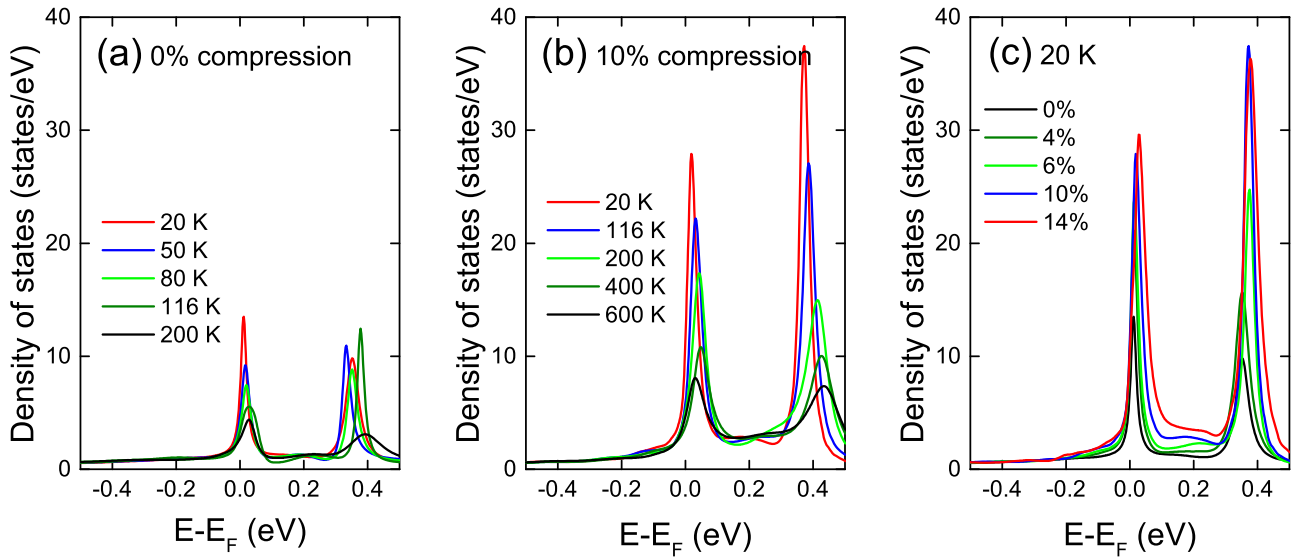


FIG. 3. Ce-4*f* density of states of CeRh₂As₂ at various temperatures and compression ratios. (a), (b) DOS at 0% and 10% volume compression, respectively, indicating the gradual formation of Kondo resonance peak with decreasing temperature. (c) Illustration of the enhancement of Kondo resonance peak with increasing compression ratio at 20 K.

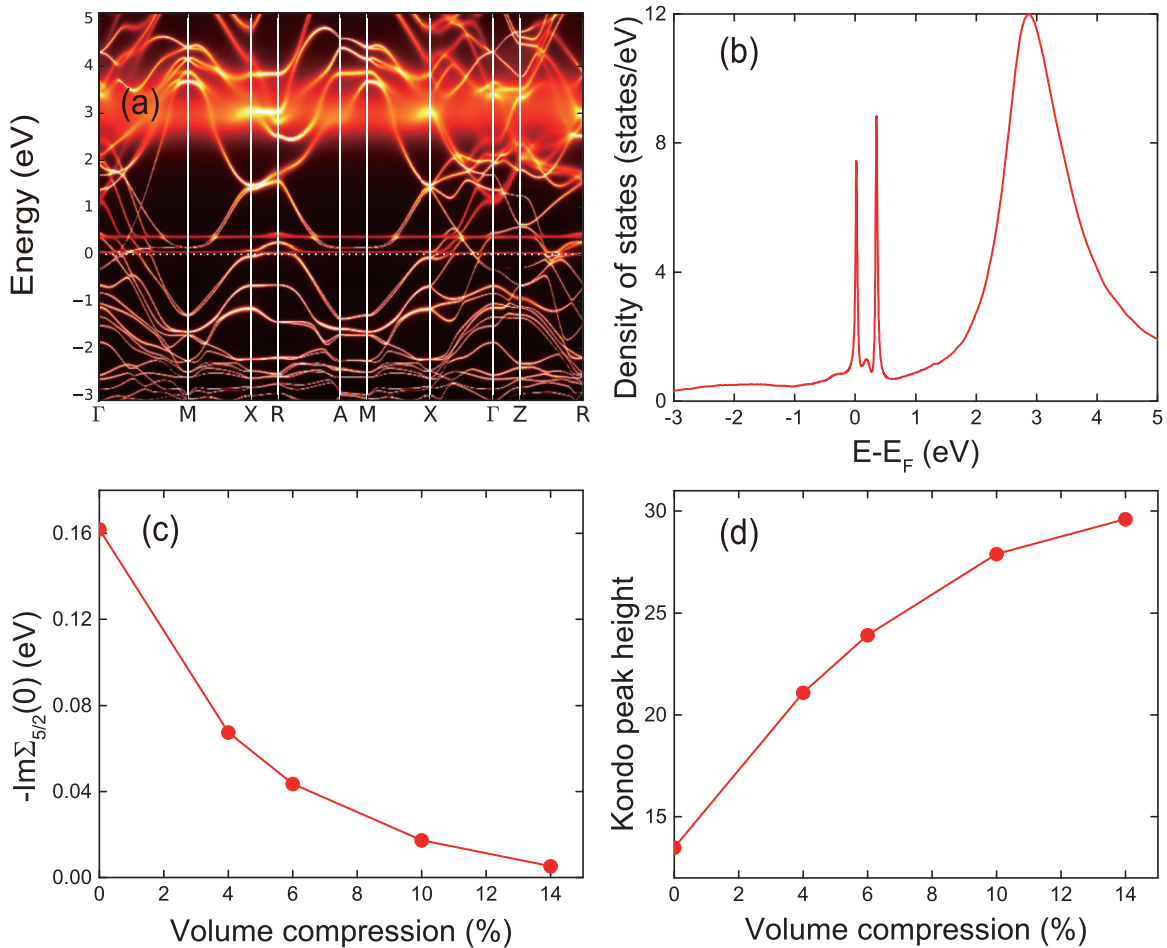


FIG. 4. (a), (b) Momentum-resolved spectral function and Ce-4*f* density of states of CeRh₂As₂ at 20 K under ambient pressure, respectively, in which the Kondo resonance peak, the lower and upper Hubbard bands can be clearly identified. (c) and (d) illustrate the zero-frequency self-energy and height of Kondo peak as functions of compression ratio at 20 K, respectively.

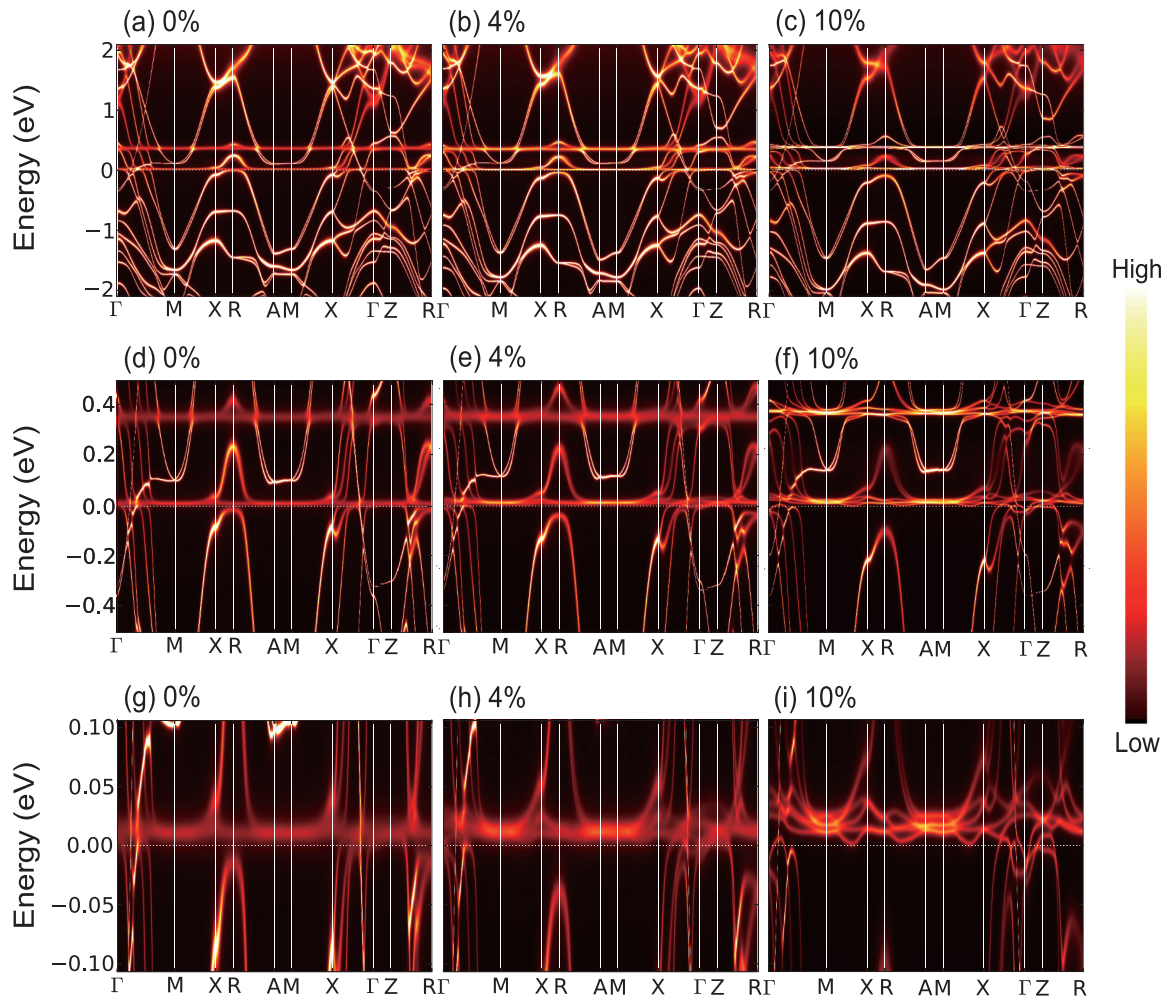


FIG. 5. DFT+DMFT momentum-resolved spectral function of CeRh_2As_2 at 20 K, under 0%, 4%, and 10% volume compressions, respectively. From top to bottom rows, the energy windows are zoomed in close to the Fermi level. The gradually distinguishable heavy-fermion bands near the Fermi level verify a localized-to-coherent crossover of Ce- $4f$ electrons under compression.

(at 27 K) starts to arise on χ_s - T curve, illustrating the onset of coherent temperature T_{coh} at which the localized-itinerant crossover occurs upon cooling [30,34]. In Figs. 4(c) and 4(d), the sharp decrease of zero-frequency self-energy and significant enhancement of Kondo-peak height between 4% to 6% volume compression further confirms the crossover to Kondo coherence. In Fig. 6(c), T_{coh} is plotted with varying compression ratios, which clearly indicates that the localized-itinerant crossover starts to emerge around 6% volume compression.

To analyze the consequence of localized-itinerant crossover to the heavy-fermion SC state, we also calculate the local spin susceptibility χ_s of nonsuperconducting CeIr_2As_2 [35,36], which is isomorphic to CeRh_2As_2 . As shown in Fig. 6(d), under ambient pressure, the temperature dependence of χ_s for CeIr_2As_2 already possesses a maximum, suggesting the itinerant nature of the Ce- $4f$ states below 35 K, which can be intuitively illustrated by the sharply dispersive heavy-fermion bands in its spectral function given in Fig. 7. The full itineration of f electrons leads to a heavy Fermi liquid state, which arises at higher pressure than the SC state in pressure-temperature phase diagram of heavy-fermion

SC compounds [37,38]. Therefore, one can speculate that the conduction of f electrons may take disadvantage of the formation of heavy-fermion superconductivity, as will be discussed in detail in the following section.

Now we turn to another recently discovered heavy-fermion SC material CeSb_2 [5]. The DFT+DMFT results are displayed in Figs. 8 and 9. In comparison with the case of CeRh_2As_2 , volume compression causes similar impacts to CeSb_2 , i.e., it reduces the imaginary Ce- $4f_{5/2}$ self-energy $-\text{Im}\Sigma_{5/2}(\omega)$ [see Fig. 8(a)], enhances the Kondo resonance peak [Fig. 8(c)] and hybridization strength [see Fig. 8(b)] remarkably, and hence eventually induces a localized-itinerant crossover at about 35 K at 20% compression rate [see the black arrow indicating the maximum of χ_s in Fig. 8(d)]. Consequently, above the critical volume compression ratio 20%, well-defined hybridization bands show up in the momentum-resolved spectral function near the Fermi level below the coherent temperature $T_{\text{coh}} = 35$ K [see Fig. 9(i)]. In contrast to CeRh_2As_2 , the critical compression rate of CeSb_2 which starts to induce localized-itinerant crossover at nonzero coherent temperature is much higher, which can be ascribed to

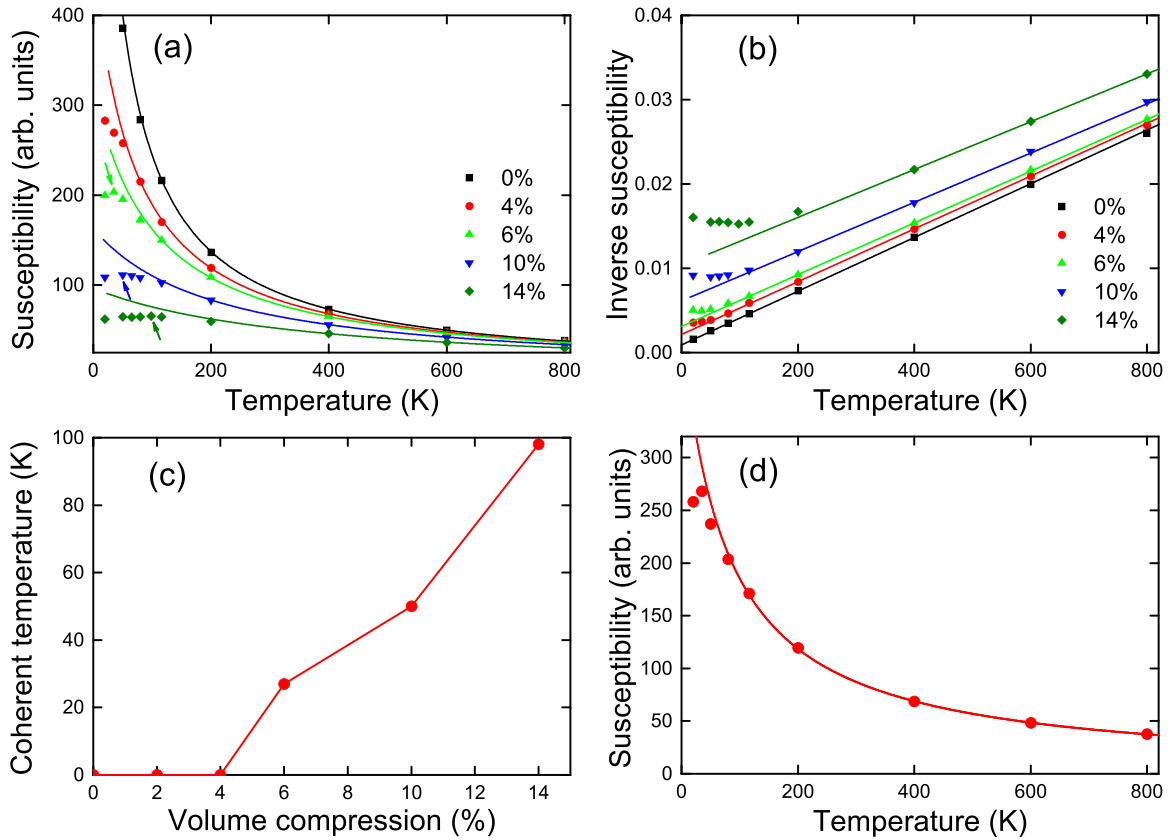


FIG. 6. Solid dots denote DFT+DMFT temperature dependence of (a) local spin susceptibility χ_s , and (b) inverse susceptibility χ_s^{-1} of CeRh_2As_2 at various volume compression rates. In (a), the arrows marking the maximum of χ_s indicate the onset of coherent temperatures, which first appears at 6% volume compression. (c) Coherent temperature T_{coh} vs volume compression percentage. (d) Temperature dependence of local spin susceptibility of CeIr_2As_2 under ambient pressure through DFT+DMFT calculation, suggesting its coherent temperature $T_{\text{coh}} \approx 35$ K. In (a), (b), and (d), the solid lines are the fitted Curis-Weiss functions.

stronger local-moment character of Ce-4*f* electrons in CeSb_2 than in CeRh_2As_2 at ambient pressure, since at 0% volume compression, the 4*f* resonance peak contributed from one Ce atom in CeSb_2 is much lower than in CeRh_2As_2 [compare Fig. 3(a) with Fig. 8(c) and note that there are many more Ce atoms in the unit cell of CeSb_2 than in CeRh_2As_2]. Different degrees of 4*f* localization can give rise to distinct ground state phases of CeRh_2As_2 and CeSb_2 at ambient pressure, as will be discussed below. In the above calculations, the crystal-field splitting (CFS) of *f* orbitals has been pre-examined and found to be one more order of magnitude smaller than SOC splitting

(several meV vs 0.36 eV) and is compatible with Kondo coherent scale. The Kondo coherent temperature T_{coh} is sensitive to the effective degeneracy of the Kondo problem, which is affected by CFS, thus by including CFS in DFT+DMFT calculations, the critical volume compression ratios in CeRh_2As_2 and CeSb_2 will be shifted, which is expected to give only a quantitative affect to the phase evolution, thus, for simplicity, CFS is not considered explicitly in the present paper [31–33], and for further studies, CFS should be included properly in DFT+DMFT calculations [39].

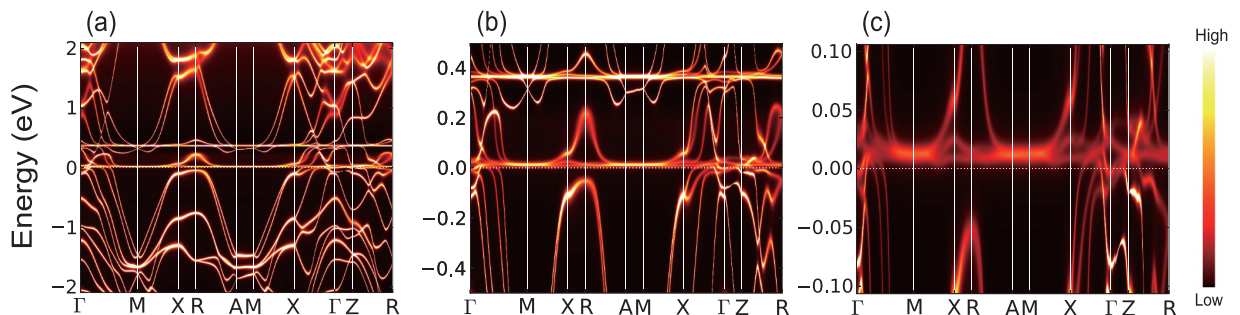


FIG. 7. DFT+DMFT momentum-resolved spectral function of CeIr_2As_2 at 20 K under ambient pressure [displayed in zoomed-in energy range near the Fermi level from (a) to (c)]. Heavy-fermion bands are already clearly resolved even at ambient pressure.

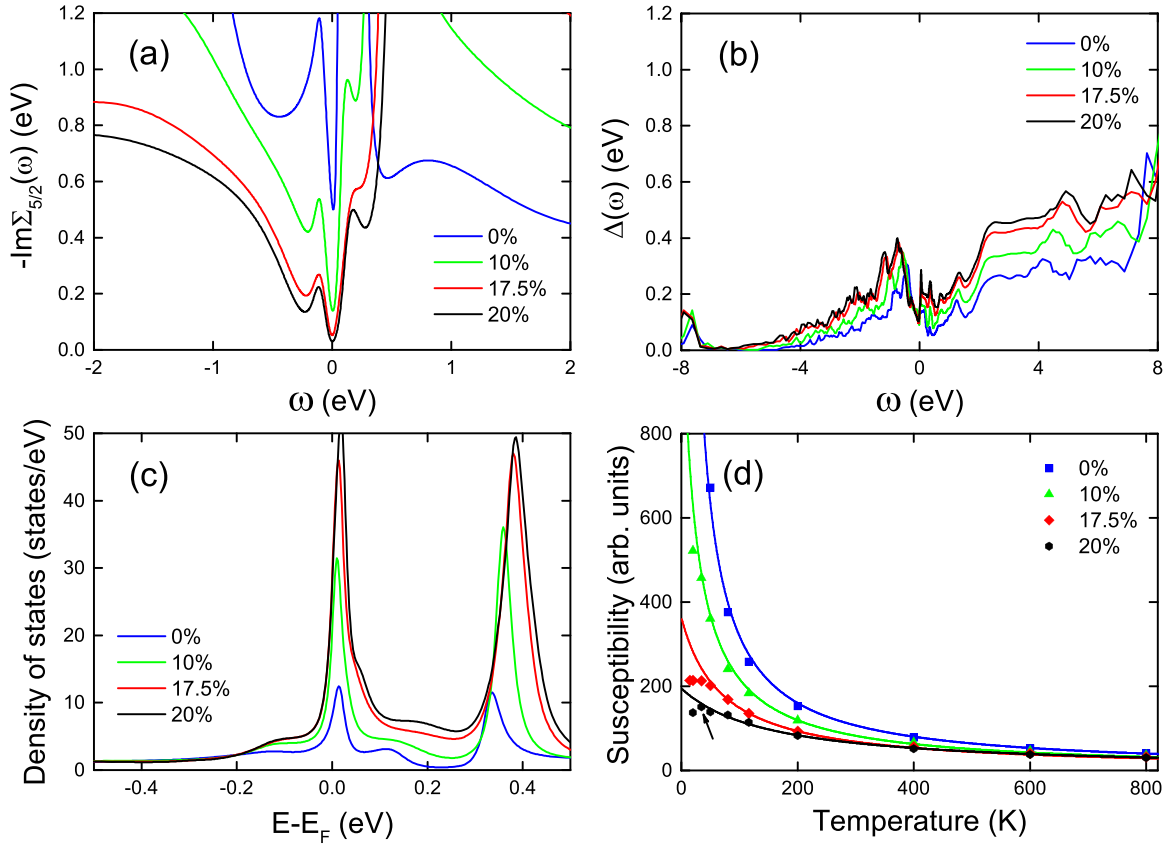


FIG. 8. (a), and (b) The real-frequency imaginary self-energy $-\text{Im}\Sigma_{5/2}(\omega)$ and hybridization function $\Delta(\omega)$ of CeSb_2 , respectively, at four compression percentages ranging from 0% to 20% at 20 K. (c) As the compression rate increases, the Kondo resonance peak near the Fermi level (at 20 K) is greatly enhanced. (d) Temperature dependence of local spin susceptibility χ_s at four volume-compression ratios. The solid dots denote DFT+DMFT results, and the solid lines are the fitted Curis-Weiss functions. In (d), the black arrow marking the maximum of χ_s indicates a coherent temperatures $T_{\text{coh}} \approx 35$ K at 20% volume compression percentage.

III. EFFECTIVE-MODEL DESCRIPTION OF PHASE EVOLUTION UNDER PRESSURE

To give a concise description concerning the general feature of the phase evolution of heavy-fermion superconductors under pressure, and to understand the consequence of the pressure-induced localized-itinerant crossover to the SC state as well, we construct a minimal effective model for heavy-fermion SC systems. Since in the heavy-fermion SC compounds we considered, Ce-4*f* electrons are mainly localized under ambient pressure, for simplicity, the role of Ce-4*f* electrons are treated as local moments as a starting point. The model Hamiltonian reads

$$\mathcal{H} = \sum_{\mathbf{k}, \sigma} \epsilon_{\mathbf{k}} c_{\mathbf{k}\sigma}^\dagger c_{\mathbf{k}\sigma} + J_K \sum_i \mathbf{S}_i \cdot \mathbf{S}_{ic} + J_H \sum_{\langle ij \rangle} \mathbf{S}_i \cdot \mathbf{S}_j, \quad (1)$$

which includes two dominating interactions in heavy-fermion systems, namely, the Kondo coupling between conducting *c* electrons and local moments with strength J_K , and the nearest-neighbor RKKY superexchange J_H term between local moments. In fact, similar simplified models have been extensively adopted in the literature and have revealed rich common features of phase transitions in heavy-fermion systems [40,41], although more precise multiorbital models should be fitted to explain experimental behaviors of individ-

ual materials. As many typical heavy-fermion SC compounds such as CeMIn_5 ($M=\text{Co}, \text{Rh}$) [Fig. 1(d)] exhibit quasi-two-dimensional Fermi surfaces [42,43], we consider above model on a two-dimensional square lattice, which can represent the arrangement of Ce atoms on the *ab* plane (see Fig. 1), with tight-binding dispersion of conduction electrons $\epsilon_{\mathbf{k}} = -2t(\cos k_x + \cos k_y) + 4t' \cos k_x \cos k_y - \mu$, in which t and t' are the nearest-neighbor and next-nearest-neighbor hopping strengths, respectively, and μ is the chemical potential for fixing conduction-electron number n_c .

In the context of *c-f* hybridization, the spin density of local moments can be expressed via slave-fermion representation as $\mathbf{S}_i = \frac{1}{2} \sum_{\alpha\beta} f_{i\alpha}^\dagger \sigma_{\alpha\beta} f_{i\beta}$, with σ being the Pauli matrix, and *f* operators are subjected to the constraint $\sum_{\sigma} f_{i\sigma}^\dagger f_{i\sigma} = 1$, imposed by adding a Lagrangian term $\sum_i \lambda_i (\sum_{\sigma} f_{i\sigma}^\dagger f_{i\sigma} - 1)$ to Eq. (1). In such representation, the RKKY interaction can be rewritten equivalently as

$$\mathbf{S}_i \cdot \mathbf{S}_j = -\frac{1}{2} (f_{i\uparrow}^\dagger f_{j\downarrow}^\dagger - f_{i\downarrow}^\dagger f_{j\uparrow}^\dagger) (f_{j\downarrow} f_{i\uparrow} - f_{j\uparrow} f_{i\downarrow}) + \frac{1}{4}, \quad (2)$$

which represents singlet-pairing interacting between neighboring *f* electrons, and can be decoupled by introducing the singlet-pairing strength

$$\Delta = \langle f_{i\uparrow}^\dagger f_{i\pm x\downarrow}^\dagger - f_{i\downarrow}^\dagger f_{i\pm x\uparrow}^\dagger \rangle = -\langle f_{i\uparrow}^\dagger f_{i\pm y\downarrow}^\dagger - f_{i\downarrow}^\dagger f_{i\pm y\uparrow}^\dagger \rangle, \quad (3)$$

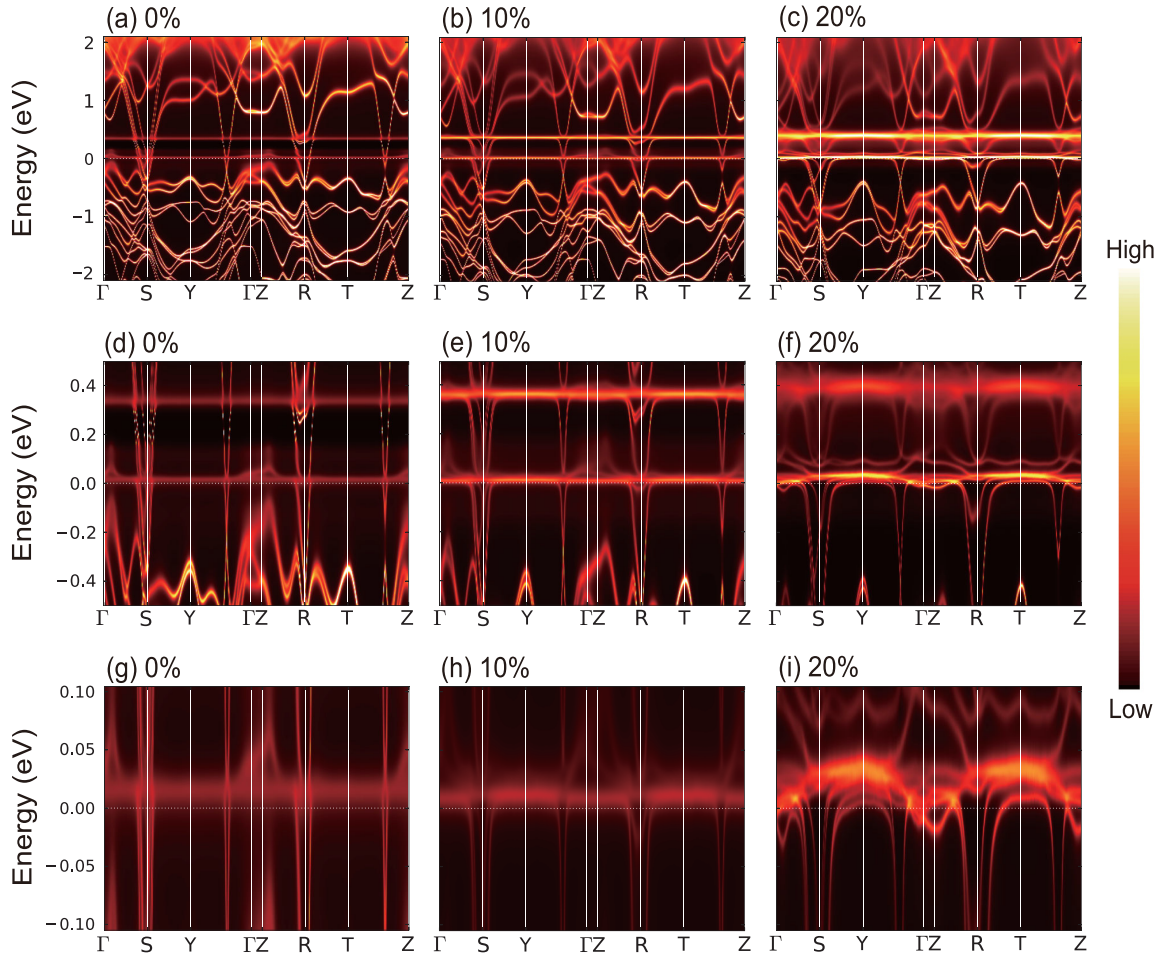


FIG. 9. Momentum-resolved spectral function of CeSb₂ at 20 K, under 0%, 10%, and 20% volume-compression ratios, respectively. From top to bottom rows, the energy ranges are zoomed in close to the Fermi level for a clearer view. The heavy-fermion bands are very distinguishable near the Fermi level at 20% compression rate.

which features $d_{x^2-y^2}$ symmetry, as many typical heavy-fermion SC systems carry d -wave symmetry in their SC pairing [25,26,44,45]. Δ is a typical form of short-range magnetic correlation and, in previous studies, it has been verified that similar magnetic correlations could induce heavy-fermion superconductivity and other unconventional superconductivity, such as SC states in cuprates and nickelates [46,47]. For heavy-fermion systems, in the presence of Kondo hybridization, the magnetic correlation can drive a paramagnetic heavy-fermion SC state [21,46], in which the SC pairing function $\langle c_{\mathbf{k}\uparrow}^\dagger c_{-\mathbf{k}\downarrow}^\dagger + c_{-\mathbf{k}\downarrow} c_{\mathbf{k}\uparrow} \rangle$ features d -wave symmetry, and the SC order parameter can be evaluated as

$$\Delta_{\text{SC}} = \frac{1}{2N} \sum_{\mathbf{k}} (\cos \mathbf{k}_x - \cos \mathbf{k}_y) \langle c_{\mathbf{k}\uparrow}^\dagger c_{-\mathbf{k}\downarrow}^\dagger + c_{-\mathbf{k}\downarrow} c_{\mathbf{k}\uparrow} \rangle. \quad (4)$$

In the following, we will show that magnetic correlation can also drive heavy-fermion SC states in the presence of AFM long-range magnetic order, leading to an AFM+SC coexisting phase in certain parameter region. Two AFM order parameters can be introduced as

$$m_c = -\frac{1}{2} \left\langle \sum_{\sigma} \sigma c_{i\sigma}^\dagger c_{i\sigma} \right\rangle e^{i\mathbf{Q}\cdot\mathbf{R}_i}, \quad m_f = \frac{1}{2} \left\langle \sum_{\sigma} \sigma f_{i\sigma}^\dagger f_{i\sigma} \right\rangle e^{i\mathbf{Q}\cdot\mathbf{R}_i}, \quad (5)$$

where $\mathbf{Q} = (\pi, \pi)$ is the AFM vector, then the staggered magnetization in the AFM state can be expressed by $M = m_f - m_c$. The Kondo coupling term can be decomposed as [48]

$$\begin{aligned} \mathbf{S}_i \cdot \mathbf{S}_{ic} = & -\frac{3}{8} (c_{i\uparrow}^\dagger f_{i\uparrow} + c_{i\downarrow}^\dagger f_{i\downarrow}) (f_{i\uparrow}^\dagger c_{i\uparrow} + f_{i\downarrow}^\dagger c_{i\downarrow}) \\ & + \frac{1}{8} (c_{i\uparrow}^\dagger f_{i\uparrow} - c_{i\downarrow}^\dagger f_{i\downarrow}) (f_{i\uparrow}^\dagger c_{i\uparrow} - f_{i\downarrow}^\dagger c_{i\downarrow}) \\ & + \frac{1}{8} (c_{i\uparrow}^\dagger f_{i\downarrow} + c_{i\downarrow}^\dagger f_{i\uparrow}) (f_{i\downarrow}^\dagger c_{i\uparrow} + f_{i\uparrow}^\dagger c_{i\downarrow}) \\ & + \frac{1}{8} (c_{i\uparrow}^\dagger f_{i\downarrow} - c_{i\downarrow}^\dagger f_{i\uparrow}) (f_{i\downarrow}^\dagger c_{i\uparrow} - f_{i\uparrow}^\dagger c_{i\downarrow}), \quad (6) \end{aligned}$$

in which the first term represents local singlet c - f hybridization, while the last three terms denote triplet hybridizations. In the presence of AFM order, the dominating c - f hybridization strength $\langle c_{i\sigma}^\dagger f_{i\sigma} \rangle$ can vary with sublattices and spin directions, leading to two different hybridization parameters $V_s = \frac{1}{2} \sum_{\sigma} \langle c_{i\sigma}^\dagger f_{i\sigma} \rangle$ and $V_t = \frac{1}{2} \sum_{\sigma} \sigma e^{i\mathbf{Q}\cdot\mathbf{R}_i} \langle c_{i\sigma}^\dagger f_{i\sigma} \rangle$, where V_s is the uniform singlet hybridization and V_t is staggered triplet hybridization, and the latter requires breaking of particle-hole symmetry of conduction electrons at presence of AFM order. Then the Kondo coupling in Eq. (6) can be treated by performing Hartree-Fock approximation using V_s and V_t . In addition, it has been shown from Monte Carlo simulations of Kondo lattice model and periodic Anderson model that Kondo coupling can naturally induce AFM order [51,52]. In the mean-field

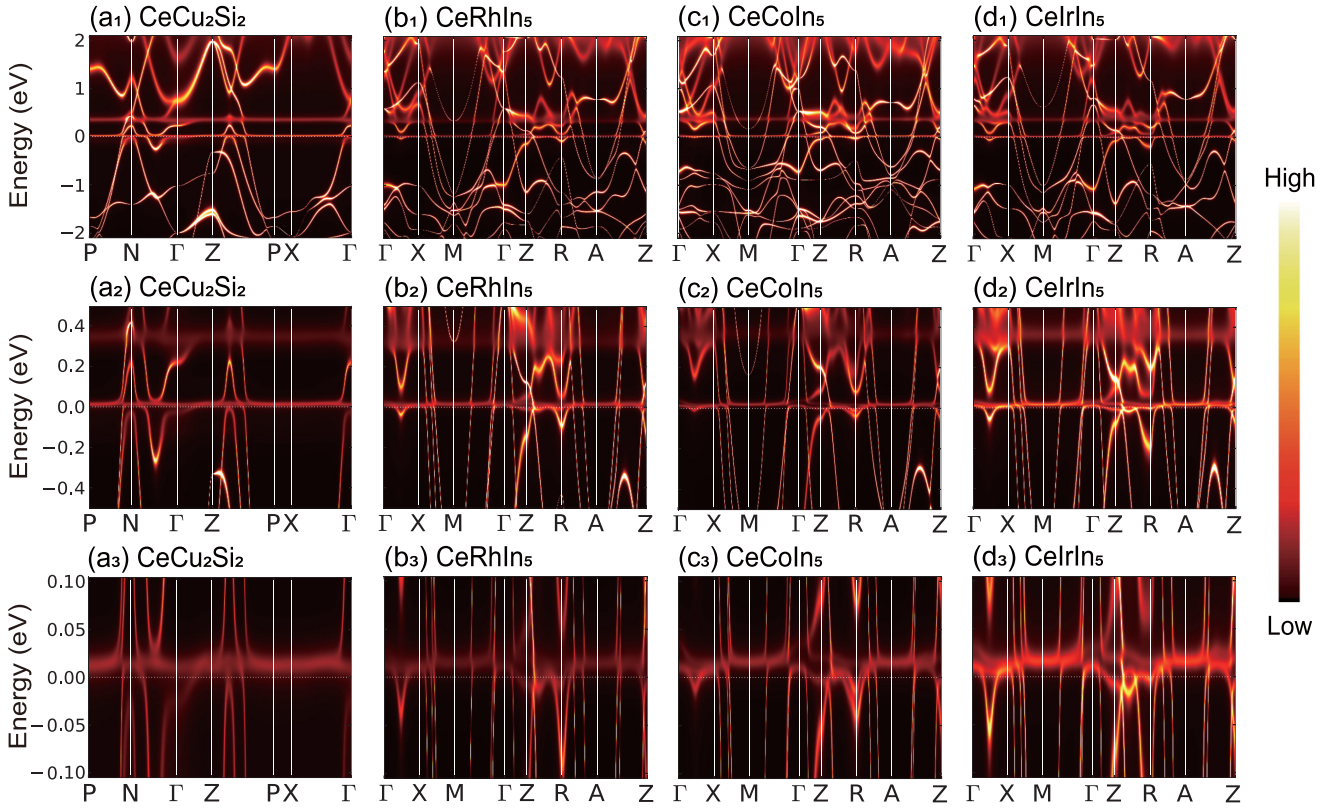


FIG. 10. Momentum-resolved spectral functions of CeCu_2Si_2 and CeMIn_5 ($M=\text{Rh, Co, Ir}$) at 20 K. From top to bottom rows, the energy windows are zoomed in close to the Fermi level. The hybridization bands of CeRhIn_5 are quite blurred, while for CeCoIn_5 and CeIrIn_5 [49,50] they become much more intense than CeRhIn_5 . The spectral weights of the hybridization bands can be roughly reflected by Ce- f density of states in Fig. 12(a).

treatment, such AFM order can be induced by decoupling the polarization term in Kondo interaction ($J_K \mathbf{S}_i^z \mathbf{S}_{ic}^z$) by substituting Eq. (5) to be

$$\sum_i \mathbf{S}_i^z \cdot \mathbf{S}_{ic}^z = -\frac{1}{2} m_c \sum_{\mathbf{k}\sigma} \sigma f_{\mathbf{k}+\mathbf{Q}\sigma}^\dagger f_{\mathbf{k}\sigma} + \frac{1}{2} m_f \sum_{\mathbf{k}\sigma} \sigma c_{\mathbf{k}+\mathbf{Q}\sigma}^\dagger c_{\mathbf{k}\sigma} + m_c m_f, \quad (7)$$

which can lead to proper description of magnetization [48,53]. For convenient, the subsequent derivation of self-consistent equations which determine the chemical potential μ , Lagrange multiplier λ , and mean-field parameters Δ , V_s , V_t , m_c , m_f , and the discussion of numerical results are given in detail in the Appendix. Based on the results of model calculations, we can draw a schematic description of heavy-fermion SC systems in Fig. 13. We find that, in addition to the Kondo hybridization (V_s and $V_t \neq 0$) between c and f electrons, the RKKY superexchange can lead to nearest-neighbor singlet pairing ($\Delta \neq 0$) between f electrons [see Fig. 13(a)], which combines with c - f hybridization to produce Cooper pairing ($\Delta_{\text{SC}} \neq 0$) between dressed heavy quasiparticles [see Fig. 13(b)], thus inducing the heavy-fermion SC state. Remarkably, even in the presence of AFM long-range magnetic order, the short-range singlet pairing can persist in some parameter regions, resulting in an AFM+SC coexisting phase with Δ_{SC} and $M \neq 0$. We have calculated the

evolution of ground-state phases with Kondo coupling J_K (see Appendix). The numerical results show that at weak Kondo coupling, long-range AFM order dominates ($M \neq 0$) and the f electrons are fully localized and decoupled with c electrons ($V_s = 0$), leading to the AFM_s phase with small Fermi surface constructed only by c electrons. While J_K increases, the c - f hybridization sets in ($V_s \neq 0$) with AFM order, leading to the AFM_L phase with a large Fermi surface forming by hybridized heavy fermions. While J_K is further enhanced, the long-range AFM order is suppressed partially, then the arising of short-range singlet pairing of f electrons ($\Delta \neq 0$) can gain lower energy than the AFM_L state and, by combining with Kondo hybridization, drives an AFM+SC coexisting phase with $\Delta_{\text{SC}}, M \neq 0$. At a critical Kondo coupling strength J_K^{c1} , the AFM order is fully suppressed, leading to an AFM magnetic transition; meanwhile, Δ survives at and above J_K^{c1} , and thus produces a paramagnetic heavy-fermion SC state beyond the magnetic transition point. Therefore, the magnetic transition at J_K^{c1} can be related to the magnetic QCP in heavy-fermion SC compounds around which the SC phase emerges [5,14,19,22]; see Fig. 13(c). In the SC phase, an increase of J_K will reduce the magnetic correlation Δ and give rise to fast reduction of SC order; see Fig. 14(a).

To track the ground-state phase evolution of realistic heavy-fermion superconductors under pressure, we combine the results of effective model with the first-principles results. In the above section, we have demonstrated that the volume compression can remarkably enhance the

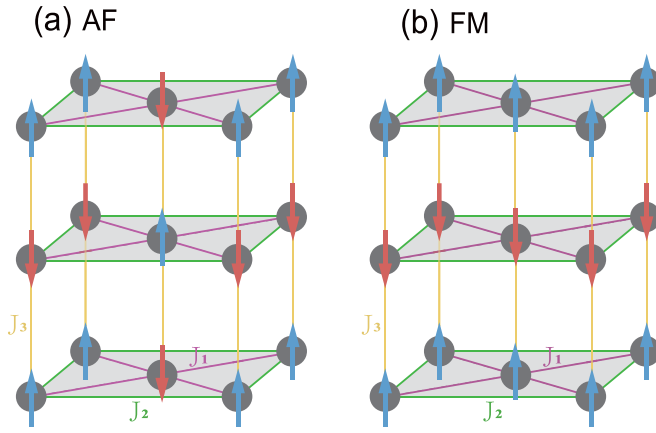


FIG. 11. DFT+ U magnetic configurations for calculating RKKY strengths in quasi-two-dimensional CeMIn_5 ($M = \text{Rh, Co, Ir}$). The solid dots represent Ce atoms with local spins. (a), (b) Intraplane AFM and FM states, respectively. The nearest-neighbor exchange J_1 corresponds to the RKKY interaction J_H to be evaluated.

hybridization function $\Delta(\omega)$ in a wide energy range [see Figs. 2(a) and 8(b)]. Figure 12(c) illustrates the averaged hybridization strength, which shows a notable enhancement with compression ratio. Since, in the Anderson impurity model, the hybridization strength Δ_{avg} and Kondo coupling J_K are

both square proportional to c - f hopping V_{cf} as $\Delta_{\text{avg}}, J_K \sim V_{cf}^2$ (by Schrieffer-Wolff transformation), Δ_{avg} can be closely related to Kondo coupling strength, thus indicating a remarkable increase of J_K with pressure. For CeCu_2Si_2 and CeMIn_5 ($M = \text{Rh, Co, Ir}$), DFT+DMFT momentum-resolved spectral functions are illustrated in Fig. 10, and corresponding $4f$ density of states are shown in Fig. 12(a). The hybridization functions of various materials are given in Fig. 12(b), with corresponding Δ_{avg} plotted in Fig. 12(d), and are also explicitly listed in Table I, which reflect their Kondo coupling strength.

To evaluate the strength of RKKY exchange J_H , we perform the DFT+ U calculations for the magnetic phases. As can be seen from the lattice structures in Fig. 1, the Ce atoms in these SC compounds are arranged into quasi-two-dimensional lattices, with intra-plane square lattice structures (slightly distorted in CeSb_2). Therefore, the largest exchange coupling between Ce atoms follows the a and b directions, which corresponds to the nearest-neighbor RKKY interaction J_H in Eq. (1). To calculate J_H , one can calculate the energy shift between different magnetic configurations using DFT+ U simulations. For simplicity, we take CeMIn_5 ($M = \text{Rh, Co, Ir}$) as an explicit example. Experimental observations have shown CeMIn_5 are AFM ordered in their ground states at ambient pressure [4,6,7]. According to the lattice structure in Fig. 1(d), due to increasing distances between Ce atoms, the next-nearest-neighbor intraplane exchange J_2

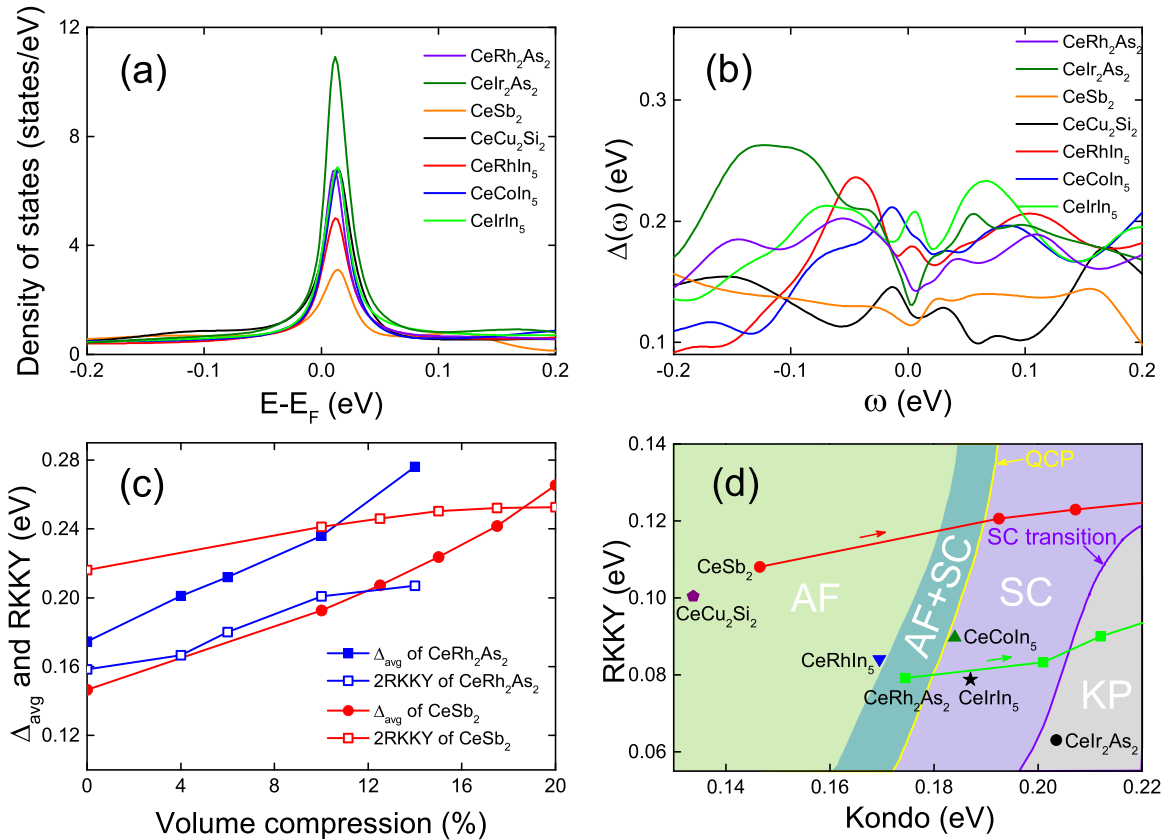


FIG. 12. (a), (b) $4f$ density of states $\rho(\omega)$ per Ce atom and the hybridization function $\Delta(\omega)$ at 20 K under ambient pressure, respectively. (c) Average hybridization Δ_{avg} and RKKY strength J_H of CeRh_2As_2 and CeSb_2 vs volume compression at 20 K. (d) Kondo coupling J_K and RKKY strength J_H in various compounds at 20 K, while the variations under compression for CeRh_2As_2 and CeSb_2 are indicated by green and red arrows, respectively. Phases and the evolution under pressure are determined through competition of J_K and J_H ; see Table I and text.

TABLE I. Kondo coupling (evaluated through average hybridization Δ_{avg}) and RKKY interaction via first-principles calculations. The predictions for ground-state phases are discussed in the text and are compared with experimental observations.

	CeRh ₂ As ₂	CeSb ₂	CeIr ₂ As ₂	CeCu ₂ Si ₂	CeRhIn ₅	CeCoIn ₅	CeIrIn ₅
Kondo (eV)	0.1745	0.147	0.2035	0.1338	0.1695	0.184	0.187
	medium	weak	strong	weak	medium-low	strong	strong
RKKY (eV)	0.0792	0.1081	0.0631	0.1004	0.0841	0.0897	0.0788
	medium	strong	weak	strong	medium	medium	medium
Kondo/2RKKY	1.102	0.681	1.613	0.666	1.01	1.03	1.19
Prediction	AFM+SC	AFM	KP	AFM	AFM	SC	SC
Experiment	AFM+SC [17,18]	AFM [5]	$T_{\text{coh}} = 35\text{K}$ KP [35]	AFM [3]	AFM [4]	SC [6]	SC [7]
			$T_{\text{coh}} = 65\text{K}$				

and interplane exchange J_3 are more successively reduced than J_H (since they decrease inversely proportional to the cube of distance), therefore, the AFM phase likely takes the configuration in Fig. 11(a), with an exchange energy of $E_{\text{AFM}} = (-8J_H + 4J_2 - 4J_3)S^2$ ($S = 1/2$, since f occupation is close to 1). To directly extract J_H , one can flip some spins to create an intraplane FM state [Fig. 11(b)] with exchange energy of $E_{\text{FM}} = (8J_H + 4J_2 - 4J_3)S^2$, thus the energy shift equals $\Delta E = E_{\text{AFM}} - E_{\text{FM}} = -16J_H S^2$. Using DFT+ U simulations for these two magnetic states (including SOC), J_H can be directly evaluated. For Ce M_2 As₂ ($M=\text{Rh, Ir}$) and CeCu₂Si₂, the local spins are also staggered on the ab plane with a displacement of $(a+b)/2$ between nearby Ce layers [18], and their J_H can be similarly determined. The resulting RKKY interactions of the ground states at ambient pressure are listed in Table I, and the pressure evolutions of J_H in CeRh₂As₂ and CeSb₂ are plotted in Figs. 12(c) and 12(d), indicating an increasing of J_H under pressure. Both J_K and J_H strengths extracted are compatible with the typical value in Ce-based materials [54].

With the estimated Kondo and RKKY interactions, the ground-state phases of these SC materials can be qualita-

tively determined according to the model results in Fig. 14(b) and are summarized on the $J_K J_H$ plane in Fig. 12(d). Due to the quasi-two-dimensional character, the average RKKY exchange energy per Ce atom equals $2J_H S^2$, thus the energy ratio between Kondo and RKKY interactions can be measured by $J_K/2J_H$ [41], which is given in Table I. For materials with weak Kondo and strong RKKY interactions (CeSb₂ and CeCu₂Si₂), RKKY interaction dominates, leading to long-range magnetic correlation, hence an AFM ordered phase; for strong Kondo and weak RKKY interactions (CeIr₂As₂, pressured CeRh₂As₂, and CeSb₂), RKKY is overwhelmed by Kondo coupling, leading to the KP phase with vanished magnetic correlation. For CeRh₂As₂ (at ambient pressure) and Ce M In₅ ($M=\text{Rh, Co, Ir}$), the magnitudes of $J_K/2J_H$ are close to 1, indicating that the magnetic correlation and Kondo hybridization are compatible, and their interplay and possible coexistence make the ground states close to the narrow AFM+SC coexisting region. Explicitly, in CeRhIn₅, the medium RKKY slightly overcomes the medium-low Kondo coupling, leading to weak AFM order near AFM+SC region; for medium RKKY and medium Kondo coupling in CeRh₂As₂, both interactions dominate, leading to the

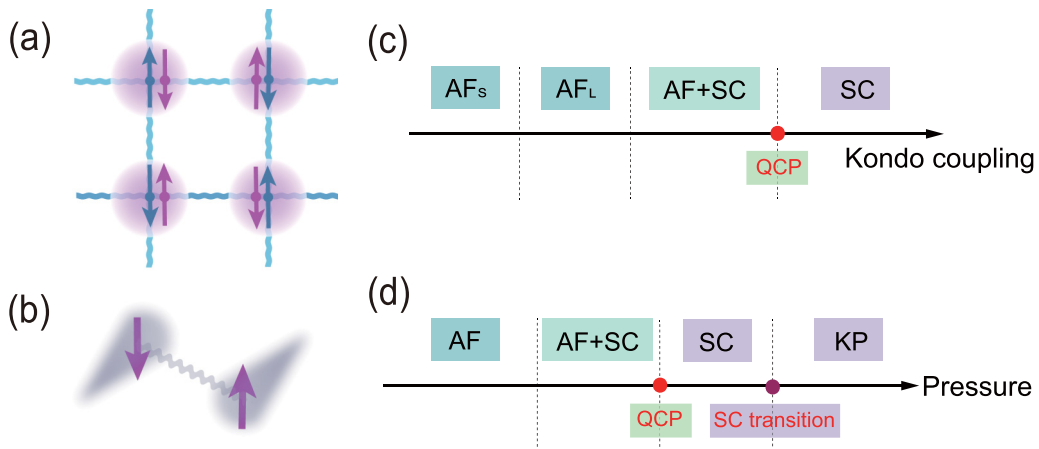


FIG. 13. Schematic description of heavy-fermion superconductor. (a) The interplay of short-range singlet pairing between f electrons (blue arrows) and Kondo screening by conduction electrons (purple arrows) drives (b) Cooper pairing between heavy quasi-particles. (c) Phase evolution in the effective model with increasing Kondo coupling. The magnetic QCP separates the SC phases into AFM+SC coexisting phase and paramagnetic SC phase. (d) Phase evolution with pressure in Ce-based superconductors. Besides the magnetic QCP, a SC transition from paramagnetic SC phase to KP phase driven by localized-itinerant crossover takes place at higher pressure. In (d), AFM_s and AFM_L states are uniformly denoted by the AFM state.

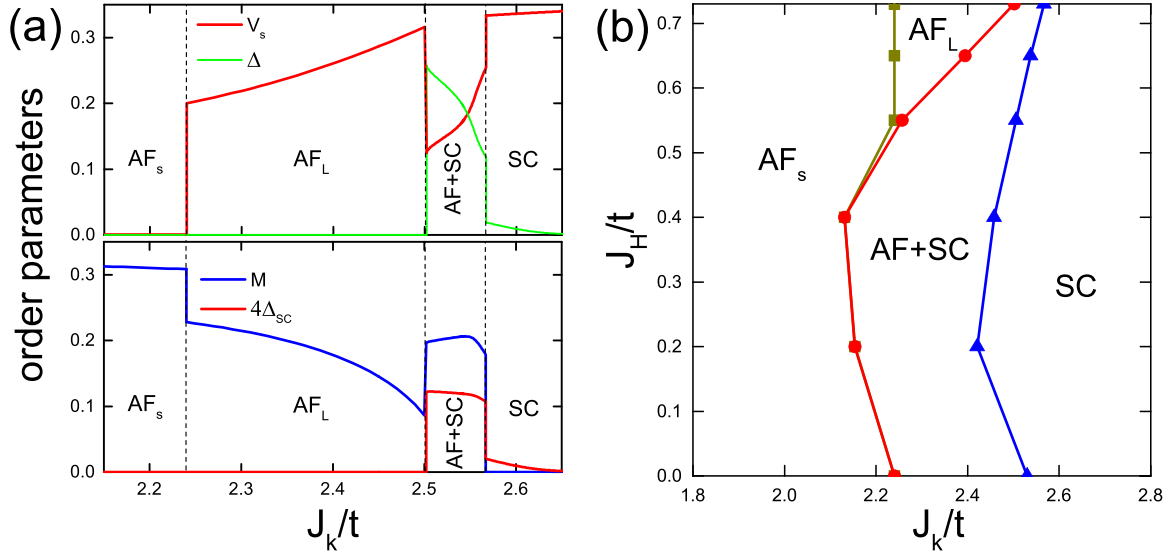


FIG. 14. (a) Variation of c - f hybridization V_s , f - f singlet pairing Δ , staggered magnetization M , and SC order Δ_{SC} as functions of Kondo coupling J_K . (b) Phase diagram of the effective model for heavy-fermion SC system. Parameters are set as $J_{K\parallel} = 0.86J_{K\perp}$, $J_{H\parallel} = 0$, $t' = 0.1$, and $n_c = 0.95$. In (a), $J_{H\perp} = 0.73$. On the horizontal and vertical axes, the magnitudes of J_K and J_H are defined according to the transverse parts $J_{K\perp}$ and $J_{H\perp}$, respectively. All energies are in units of nearest-neighbor hopping strength t between conduction electrons.

AFM+SC coexisting phase; while for CeCoIn₅ and CeIrIn₅ with medium RKKY and strong Kondo interactions, Kondo hybridization coexists with residual short-range magnetic correlation, resulting in a paramagnetic heavy-fermion SC phase. It should be noted that in the model results in Fig. 14(b), J_K and J_H are in units of t , and also due to the simplification of the effective model (neglecting the three-dimensional structure and interplane exchanges in these materials, etc.), for CeRh₂As₂ (at ambient pressure) and CeMIn₅ (M =Rh, Co, Ir), which have compatible J_K and J_H , the phases may not be precisely located. Despite that, their relative positions on the evolution path [Fig. 13(d)] can be correctly determined; see Fig. 12(d).

As shown in Fig. 12(c), volume compression significantly enhances both Kondo and RKKY strengths [41] in CeRh₂As₂ and CeSb₂, nevertheless, the growth of Kondo coupling seems to be more rapid than RKKY. During the competition, Kondo interaction gradually overwhelms RKKY interaction and dominates at high pressure; consequently, the magnetic correlations between Ce atoms are suppressed. The evolutions of J_K and J_H under compression are indicated by green and red arrows for CeRh₂As₂ and CeSb₂ in Fig. 12(d), respectively. By comparison with Fig. 14(b), due to much slower enhancement of J_H than J_K under pressure, the phase evolutions follow similar path in Fig. 14(a), i.e., from AFM to AFM+SC, then to the SC phase, starting from different ground states at ambient pressure (AFM and AFM+SC for CeSb₂ and CeRh₂As₂, respectively). Moreover, further increase of pressure causes the localized-itinerant crossover at critical pressure P_c at which the f electrons become fully itinerant. As a consequence, the magnetic correlation Δ between f electrons eventually vanishes at P_c due to overwhelming J_K over J_H , and hence destructs the heavy-fermion SC state and induces a further SC-to-KP transition at P_c . The SC-to-KP transition can be qualitatively located near the Kondo-coherent CeIr₂As₂, 6% compressed CeRh₂As₂ and near 20% compressed CeSb₂, at

which they undergo localized-itinerant transitions, see the purple line in Fig. 12(d). Since the f electrons are simply described by local moments in the effective model, the localized-itinerant crossover and corresponding SC-KP transition may not be directly obtained in the model level, nevertheless, such SC transition can still be understood by the ignorable SC order Δ_{SC} at large J_K [see Fig. 14(a), Δ_{SC} decreases rapidly above $J_K = 2.6t$], on the right side of SC phase in Fig. 14(b).

Based on above analysis of the effective-model and first-principles calculations, we have depicted a qualitative description regarding the commonality in phase-evolution processes of heavy-fermion SC compounds under pressure. In general, with increasing pressure, these compounds follow a similar path in Fig. 13(d), however, they start at distinct ground-state phases at ambient pressure, depending on the competition between Kondo and RKKY interactions. With increasing pressure, two notable transitions take place successively, one is the magnetic QCP, the other is the SC-KP transition. The QCP corresponds to the AFM transition which separates the SC states into AFM+SC coexisting phase and paramagnetic SC phase [see the yellow line in Fig. 12(d)], while the SC transition is induced by the localized-itinerant crossover of f electrons, which eliminates the magnetic correlation hence destructs heavy-fermion SC state and produces a KP phase thereafter.

IV. CONCLUSION AND DISCUSSION

To summarize, based on comprehensive studies of typical Ce-based superconductors via combining first-principles simulations with effective-model calculations, we have presented a proper description regarding their paths of phase evolutions under pressure. Particularly, we have demonstrated that at the presence of c - f hybridization, the short-range singlet pairing between f electrons in the context of AFM

long-range order can drive a notable AFM+SC coexisting phase, which is separated with paramagnetic SC phase by a magnetic transition, and thus gives a natural explanation to the observed magnetic QCP inside the SC phases. Furthermore, the crossover from localization to itineration for f electrons under increasing pressure gives a theoretical interpretation for the SC-to-KP transition in these SC compounds at high pressure. By examining the degree of Kondo coupling and RKKY superexchange in these materials, we have eventually depicted a schematic phase diagram with respect to the pressure dependence of their ground-state phases from ambient pressure. Our description for the ground states of heavy-fermion SC systems are consistent with the phenomenological two-fluid theory [27,28], and may help to achieve a microscopic explanation for the pressure-temperature phase diagram.

Although our method gives an appropriate description regarding the main feature of the phase evolutions in typical Ce-based heavy-fermions SC materials under pressure, the explicit processes may differ, e.g., other than d -wave symmetry [25,26], the SC pairing symmetries can be s_{\pm} wave [55] or nodeless mixing-type d wave [56]. Besides, in CeRh₂As₂ and other noncentrosymmetric SC compounds [57], the mixing of spin-singlet and triplet pairings may induce the transition or mixing between even and odd parities under pressure [17]. In addition, under higher pressure above the SC transition point, a distinct SC state can arise in CeCu₂Si₂, which may be induced by valence-electron fluctuation or orbital transition [3,58]. Moreover, besides the SC pairing mediated by magnetic correlation, other SC pairing mechanisms can also work, such as Kondo-destruction QCP [59] and quadrupolar-exciton-mediated pairing in PrOs₄Sb₁₂ [60]. Therefore, the explicit theoretical explanations for the pressure dependence of these distinct heavy-fermion SC systems require extended studies beyond our minimal effective model. Our paper can also help one to understand the heavy-fermion SC states emerging around the ferromagnetic quantum transition point in UCoGe and UGe₂ [61,62].

ACKNOWLEDGMENTS

H.L. and Y.L. are grateful to earlier guidance and collaboration with G. M. Zhang. This work is supported by National Natural Science Foundation of China (No. 12364023), Guangxi Natural Science Foundation (No. 2024GXNS-FAA010273) and the National Key Research and Development Program of China (No. 2021YFB3501503).

APPENDIX: DETAILS OF MODEL CALCULATION

Based on the mean-field schedule described in Sec. III, and in consideration of the longitudinal polarization terms in Kondo coupling and RKKY interaction, the model Hamiltonian is written in momentum space as

$$\begin{aligned} \mathcal{H} = & \sum_{\mathbf{k},\sigma} \epsilon_{\mathbf{k}} c_{\mathbf{k}\sigma}^{\dagger} c_{\mathbf{k}\sigma} + \sum_{\mathbf{k},\sigma} \lambda f_{\mathbf{k}\sigma}^{\dagger} f_{\mathbf{k}\sigma} \\ & + \sum_{\mathbf{k}} \Delta_{\mathbf{k}} (f_{\mathbf{k}\uparrow}^{\dagger} f_{-\mathbf{k}\downarrow}^{\dagger} + \text{H. c.}) \\ & + \frac{1}{2} J_{K\parallel} m_f \sum_{\mathbf{k}\sigma} \sigma c_{\mathbf{k}+\mathbf{Q}\sigma}^{\dagger} c_{\mathbf{k}\sigma} - m \sum_{\mathbf{k}\sigma} \sigma f_{\mathbf{k}+\mathbf{Q}\sigma}^{\dagger} f_{\mathbf{k}\sigma} \end{aligned}$$

$$\begin{aligned} & - \frac{1}{4} J_{K\perp} \sum_{\mathbf{k}\sigma} (3V_s f_{\mathbf{k}\sigma}^{\dagger} c_{\mathbf{k}\sigma} - V_t \sigma c_{\mathbf{k}\sigma}^{\dagger} f_{\mathbf{k}+\mathbf{Q}\sigma} + \text{H.c.}) \\ & + N \left[\frac{1}{2} J_{K\perp} (3V_s^2 - V_t^2) + J_{H\perp} \Delta^2 + J_{K\parallel} m_c m_f \right. \\ & \left. + 2J_{H\parallel} m_f^2 - \lambda \right], \end{aligned} \quad (\text{A1})$$

where $\Delta_{\mathbf{k}} = -J_{H\perp} \Delta (\cos \mathbf{k}_x - \cos \mathbf{k}_y)$, $m = 2J_{H\parallel} m_f + \frac{1}{2} J_{K\parallel} m_c$, and N is the total number of lattice sites. In above equation, the strengths of transverse channels ($J_{K\perp}$, $J_{H\perp}$) and longitudinal channels ($J_{K\parallel}$, $J_{H\parallel}$) in both Kondo coupling and RKKY interaction are treated independently for better performance. By defining a Nambu operator $\Phi_{\mathbf{k}} = (c_{\mathbf{k}\uparrow} c_{\mathbf{k}+\mathbf{Q}\uparrow} c_{-\mathbf{k}\downarrow}^{\dagger} c_{-\mathbf{k}+\mathbf{Q}\downarrow}^{\dagger} f_{\mathbf{k}\uparrow} f_{\mathbf{k}+\mathbf{Q}\uparrow} f_{-\mathbf{k}\downarrow}^{\dagger} f_{-\mathbf{k}+\mathbf{Q}\downarrow}^{\dagger})^T$, the mean-field Hamiltonian Eq. (A1) is rewritten in a compact form as $\mathcal{H} = N\eta + \sum_{\mathbf{k}} \Phi_{\mathbf{k}}^{\dagger} \mathbf{H}_{\mathbf{k}} \Phi_{\mathbf{k}}$, in which the summation of \mathbf{k} is now restricted in the AFM magnetic Brillouin zone, with $\eta = \frac{1}{2} J_{K\perp} (3V_s^2 - V_t^2) + J_{H\perp} \Delta^2 + J_{K\parallel} m_c m_f + 2J_{H\parallel} m_f^2 - \mu + \mu n_c$, and the Hamiltonian matrix

$$\mathbf{H}_{\mathbf{k}} = \begin{pmatrix} \mathbf{A}_{\mathbf{k}} & \mathbf{V} \\ \mathbf{V} & \mathbf{B}_{\mathbf{k}} \end{pmatrix}, \quad (\text{A2})$$

with

$$\mathbf{A}_{\mathbf{k}} = \begin{pmatrix} \epsilon_{\mathbf{k}} & \frac{1}{2} J_{K\parallel} m_f & 0 & 0 \\ \frac{1}{2} J_{K\parallel} m_f & \epsilon_{\mathbf{k}+\mathbf{Q}} & 0 & 0 \\ 0 & 0 & -\epsilon_{\mathbf{k}} & \frac{1}{2} J_{K\parallel} m_f \\ 0 & 0 & \frac{1}{2} J_{K\parallel} m_f & -\epsilon_{\mathbf{k}+\mathbf{Q}} \end{pmatrix}, \quad (\text{A3})$$

$$\mathbf{V} = \begin{pmatrix} -\frac{3}{4} J_{K\perp} V_s & \frac{1}{4} J_{K\perp} V_t & 0 & 0 \\ \frac{1}{4} J_{K\perp} V_t & -\frac{3}{4} J_{K\perp} V_s & 0 & 0 \\ 0 & 0 & \frac{3}{4} J_{K\perp} V_s & \frac{1}{4} J_{K\perp} V_t \\ 0 & 0 & \frac{1}{4} J_{K\perp} V_t & \frac{3}{4} J_{K\perp} V_s \end{pmatrix}, \quad (\text{A4})$$

$$\mathbf{B}_{\mathbf{k}} = \begin{pmatrix} \lambda & -m & \Delta_{\mathbf{k}} & 0 \\ -m & \lambda & 0 & -\Delta_{\mathbf{k}} \\ \Delta_{\mathbf{k}} & 0 & -\lambda & -m \\ 0 & -\Delta_{\mathbf{k}} & -m & -\lambda \end{pmatrix}. \quad (\text{A5})$$

In general, the quasiparticle spectrums have to be obtained by numerical diagonalization of $\mathbf{H}_{\mathbf{k}}$ via $\mathbf{U}_{\mathbf{k}}^{\dagger} \mathbf{H}_{\mathbf{k}} \mathbf{U}_{\mathbf{k}} = \Lambda_{\mathbf{k}} = \text{diag}(E_{\mathbf{k}}^{(1)}, E_{\mathbf{k}}^{(2)}, \dots, E_{\mathbf{k}}^{(8)})$, in which $\mathbf{U}_{\mathbf{k}}$ is a unitary matrix, and can be extracted through numerical diagonalization. Therefore, by transforming Nambu operator $\Phi_{\mathbf{k}}$ to the quasiparticle operator $\Psi_{\mathbf{k}}$ by $\Phi_{\mathbf{k}} = \mathbf{U}_{\mathbf{k}} \Psi_{\mathbf{k}}$, with $\Psi_{\mathbf{k}}^{\dagger} = (\Psi_{\mathbf{k}}^{(1)\dagger}, \dots, \Psi_{\mathbf{k}}^{(8)\dagger})$, the matrix expression of Hamiltonian is written as $\Phi_{\mathbf{k}}^{\dagger} \mathbf{H}_{\mathbf{k}} \Phi_{\mathbf{k}} = \Psi_{\mathbf{k}}^{\dagger} \Lambda_{\mathbf{k}} \Psi_{\mathbf{k}}$ in a diagonalized form. Now one can evaluate the ground-state expectation values for quadratic products of d and f operators through ($n, m = 1, \dots, 8$)

$$\begin{aligned} \langle nm \rangle_{\mathbf{k}} & \equiv \langle (\Phi_{\mathbf{k}}^{\dagger})_n (\Phi_{\mathbf{k}})_m \rangle \\ & = \sum_{i,j} (\mathbf{U}_{\mathbf{k}})_{ni}^* (\mathbf{U}_{\mathbf{k}})_{mj} \langle \Psi_{\mathbf{k}}^{(i)\dagger} \Psi_{\mathbf{k}}^{(j)} \rangle \\ & = \sum_i (\mathbf{U}_{\mathbf{k}})_{ni}^* (\mathbf{U}_{\mathbf{k}})_{mi} \Theta(-E_{\mathbf{k}}^{(i)}). \end{aligned} \quad (\text{A6})$$

Consequently, the self-consistent equations determining the chemical potential μ , Lagrangian multiplier λ , and mean-field parameters Δ , V_s , V_t , m_c , m_f can be derived via

$$n_c = \frac{1}{N} \sum_{\mathbf{k}\sigma} \langle c_{\mathbf{k}\sigma}^\dagger c_{\mathbf{k}\sigma} + c_{\mathbf{k}+\mathbf{Q}\sigma}^\dagger c_{\mathbf{k}+\mathbf{Q}\sigma} \rangle, \quad (\text{A7})$$

$$1 = \frac{1}{N} \sum_{\mathbf{k}\sigma} \langle f_{\mathbf{k}\sigma}^\dagger f_{\mathbf{k}\sigma} + f_{\mathbf{k}+\mathbf{Q}\sigma}^\dagger f_{\mathbf{k}+\mathbf{Q}\sigma} \rangle, \quad (\text{A8})$$

$$m_c = -\frac{1}{2N} \sum_{\mathbf{k}\sigma} \sigma \langle c_{\mathbf{k}\sigma}^\dagger c_{\mathbf{k}+\mathbf{Q}\sigma} + c_{\mathbf{k}+\mathbf{Q}\sigma}^\dagger c_{\mathbf{k}\sigma} \rangle, \quad (\text{A9})$$

$$m_f = \frac{1}{2N} \sum_{\mathbf{k}\sigma} \sigma \langle f_{\mathbf{k}\sigma}^\dagger f_{\mathbf{k}+\mathbf{Q}\sigma} + f_{\mathbf{k}+\mathbf{Q}\sigma}^\dagger f_{\mathbf{k}\sigma} \rangle, \quad (\text{A10})$$

$$\Delta = \frac{1}{2N} \sum_{\mathbf{k}} (\cos \mathbf{k}_x - \cos \mathbf{k}_y) \langle f_{\mathbf{k}\uparrow}^\dagger f_{-\mathbf{k}\downarrow}^\dagger - f_{-\mathbf{k}\downarrow}^\dagger f_{\mathbf{k}\uparrow}^\dagger - f_{\mathbf{k}+\mathbf{Q}\uparrow}^\dagger f_{-\mathbf{k}+\mathbf{Q}\downarrow}^\dagger + f_{-\mathbf{k}+\mathbf{Q}\downarrow}^\dagger f_{\mathbf{k}+\mathbf{Q}\uparrow}^\dagger \rangle, \quad (\text{A11})$$

$$\mathbf{V}_s = \frac{1}{2N} \sum_{\mathbf{k}} \langle c_{\mathbf{k}\uparrow}^\dagger f_{-\mathbf{k}\uparrow} + c_{\mathbf{k}+\mathbf{Q}\uparrow}^\dagger f_{\mathbf{k}+\mathbf{Q}\uparrow} + c_{-\mathbf{k}\downarrow}^\dagger f_{-\mathbf{k}\downarrow} + c_{-\mathbf{k}+\mathbf{Q}\downarrow}^\dagger f_{-\mathbf{k}+\mathbf{Q}\downarrow} \rangle, \quad (\text{A12})$$

$$\mathbf{V}_t = \frac{1}{2N} \sum_{\mathbf{k}} \langle c_{\mathbf{k}\uparrow}^\dagger f_{\mathbf{k}+\mathbf{Q}\uparrow} + c_{\mathbf{k}+\mathbf{Q}\uparrow}^\dagger f_{\mathbf{k}\uparrow} - c_{-\mathbf{k}\downarrow}^\dagger f_{-\mathbf{k}+\mathbf{Q}\downarrow} - c_{-\mathbf{k}+\mathbf{Q}\downarrow}^\dagger f_{-\mathbf{k}\downarrow} \rangle \quad (\text{A13})$$

by substituting Eq. (A6). Note that \mathbf{k} summations in the above equations are confined in the magnetic Brillouin zone. Equations (A7)–(A13) are then solved self-consistently through numerical iterations.

In Sec. II, we demonstrated that pressure can remarkably enhance the Kondo coupling strength in heavy-fermion SC compounds; thus, based on the effective model, we first calculate the variation of order parameters as functions of Kondo coupling strength J_K , and the results are illustrated in Fig. 14(a). Under proper magnitude of RKKY interaction J_H , the Kondo hybridization V_s , staggered magnetization $M = m_f - m_c$, and SC order parameter Δ_{SC} evolve along a representative path. At weak Kondo coupling J_K , long-range magnetic correlation dominates; meanwhile, the Kondo hybridizations V_s and V_t vanish, leading to an AFM phase ($M \neq 0$) with a small Fermi surface occupied only by conduction electrons (denoted by AFM_s). While $2.24t < J_K < 2.502t$, c - f hybridizations set in ($V_s, V_t \neq 0$) and coexist with AFM

long-range order, leading to another AFM phase with large Fermi surface constructed by both c and f electrons (denoted by AFM_L). With strong Kondo coupling ($J_K > 2.567t$), the AFM long-range order is fully suppressed, however, the short-range magnetic correlation Δ survives and coexists with Kondo hybridization V_s , driving a paramagnetic d -wave SC state with nonvanishing SC order $\Delta_{\text{SC}} \neq 0$, in which the SC pairing is caused by heavy quasiparticles combining c with f electrons [46]. Notably, in the intermediate region of Kondo coupling ($2.502t < J_K < 2.567t$), a novel phase emerges, which coexists AFM order ($M \neq 0$, meanwhile the short-range magnetic correlation persists) with heavy-fermion SC pairing ($V_s, \Delta_{\text{SC}} \neq 0$), and can be ascribed to the AFM+SC phases observed in some Ce-based heavy-fermion materials such as CeCu₂Si₂, CeRhIn₅, CeSb₂, and CeRh₂As₂ under ambient or high pressures [3–5,17].

In summation of the evolution process with Kondo coupling strength, three notable transitions arise as a consequence of competition between Kondo hybridization and magnetic correlation, and the resulting phase diagram is plotted on the J_K - J_H plane in Fig. 14(b). First, the enhancement of Kondo hybridization V_s (under increasing J_K) reduces the long-range AFM order and drives a magnetic transition denoted by the blue solid line in Fig. 14(b), which divides the SC states into an AFM+SC phase and paramagnetic SC phase, respectively. Although long-range AFM order is already diminished in the paramagnetic SC state, short-range magnetic correlation Δ survives and drives the paramagnetic heavy-fermion SC state in company with Kondo hybridization. Second, while Kondo coupling J_K is further reduced in the AFM+SC phase, the long-range AFM order gains lower energy than the short-range singlet correlation, hence a SC transition occurs at which Δ vanishes, denoted by the red line in Fig. 14(b). Continual decreasing of Kondo coupling reduces the Kondo hybridization V_s , and eventually produces a Fermi-surface reconstruction in the AFM states from large to small Fermi surfaces at which V_s vanishes, indicated by the dark yellow line in Fig. 14(b). It should be noted that the present calculation gives a first-order AFM transition between AFM+SC phase and paramagnetic SC phase in Fig. 14(b), owing to our setting of model parameters which deviates from particle-hole symmetry to make the transition more noticeable. Such first-order magnetic transition is similar to that observed in CeIn₃ under pressure [11]. In addition, the magnetic transition can be continuous under particle-hole symmetric setting of model parameters [48], which can give explanation to the magnetic QCP of CePd₂Si₂ and CeCu₂Si₂ under pressure [22].

- [1] K. Andres, J. E. Graebner, and H. R. Ott, *Phys. Rev. Lett.* **35**, 1779 (1975).
 [2] F. Steglich, J. Aarts, C. D. Bredl, W. Lieke, D. Meschede, W. Franz, and H. Schäfer, *Phys. Rev. Lett.* **43**, 1892 (1979).
 [3] H. Q. Yuan, F. M. Grosche, M. Deppe, C. Geibel, G. Sparn, and F. Steglich, *Science* **302**, 2104 (2003).
 [4] Y. Ida, R. Settai, Y. Ota, F. Honda, and Y. Ōnuki, *J. Phys. Soc. Jpn.* **77**, 084708 (2008).

- [5] O. P. Squire, S. A. Hodgson, J. Chen, V. Fedoseev, C. n K. de Podesta, T. I. Weinberger, P. L. Alireza, and F. Malte Grosche, [arXiv:2211.00975](https://arxiv.org/abs/2211.00975).
 [6] V. A. Sidorov, M. Nicklas, P. G. Pagliuso, J. L. Sarrao, Y. Bang, A. V. Balatsky, and J. D. Thompson, *Phys. Rev. Lett.* **89**, 157004 (2002).
 [7] T. Shang, R. E. Baumbach, K. Gofryk, F. Ronning, Z. F. Weng, J. L. Zhang, X. Lu, E. D. Bauer, J. D. Thompson, and H. Q. Yuan, *Phys. Rev. B* **89**, 041101(R) (2014).

- [8] S. Khim, J. F. Landaeta, J. Banda, N. Bannor, M. Brando, P. M. R. Brydon, D. Hafner, R. K uchler, R. Cardoso-Gil, U. Stockert, A. P. Mackenzie, D. F. Agterberg, C. Geibel, and E. Hassinger, *Science* **373**, 1012 (2021).
- [9] C. Pfeleiderer, *Rev. Mod. Phys.* **81**, 1551 (2009).
- [10] B. D. White, J. D. Thompson, and M. B. Maple, *Physica C* **514**, 246 (2015).
- [11] S. Kawasaki, M. Yashima, Y. Kitaoka, K. Takeda, K. Shimizu, Y. Oishi, M. Takata, T. C. Kobayashi, H. Harima, S. Araki, H. Shishido, R. Settai, and Y.  nuki, *Phys. Rev. B* **77**, 064508 (2008).
- [12] P. G. Pagliuso, C. Petrovic, R. Movshovich, D. Hall, M. F. Hundley, J. L. Sarrao, J. D. Thompson, and Z. Fisk, *Phys. Rev. B* **64**, 100503(R) (2001).
- [13] S. Nair, O. Stockert, U. Witte, M. Nicklas, R. Schedler, K. Kiefer, J. D. Thompson, A. D. Bianchi, Z. Fisk, S. Wirth, and F. Steglich, *Proc. Natl. Acad. Sci. USA* **107**, 9537 (2010).
- [14] T. Park, F. Ronning, H. Q. Yuan, M. B. Salamon, R. Movshovich, J. L. Sarrao, and J. D. Thompson, *Nature (London)* **440**, 65 (2006).
- [15] V. A. Sidorov, X. Lu, T. Park, H. Lee, P. H. Tobash, R. E. Baumbach, F. Ronning, E. D. Bauer, and J. D. Thompson, *Phys. Rev. B* **88**, 020503(R) (2013).
- [16] R. Movshovich, T. Graf, D. Mandrus, J. D. Thompson, and J. L. Smith, and Z. Fisk, *Phys. Rev. B* **53**, 8241 (1996).
- [17] H. Siddiquee, Z. Rehfuss, C. Broyles, and S. Ran, *Phys. Rev. B* **108**, L020504 (2023).
- [18] M. Kibune, S. Kitagawa, K. Kinjo, S. Ogata, M. Manago, T. Taniguchi, K. Ishida, M. Brando, E. Hassinger, H. Rosner, C. Geibel, and S. Khim, *Phys. Rev. Lett.* **128**, 057002 (2022).
- [19] A. J. Millis, *Phys. Rev. B* **48**, 7183 (1993).
- [20] D. J. Scalapino, *Rev. Mod. Phys.* **84**, 1383 (2012).
- [21] J. S. Van Dyke, F. Masee, M. P. Allan, J. C. S eamus Davis, C. Petrovic, and D. K. Morr, *Proc. Natl. Acad. Sci. USA* **111**, 11663 (2014).
- [22] J. Arndt, O. Stockert, K. Schmalzl, E. Faulhaber, H. S. Jeevan, C. Geibel, W. Schmidt, M. Loewenhaupt, and F. Steglich, *Phys. Rev. Lett.* **106**, 246401 (2011).
- [23] N. D. Mathur, F. M. Grosche, S. R. Julian, I. R. Walker, D. M. Freye, R. K. W. Haselwimmer, and G. G. Lonzarich, *Nature (London)* **394**, 39 (1998).
- [24] N. Andrei and P. Coleman, *Phys. Rev. Lett.* **62**, 595 (1989).
- [25] K. An, T. Sakakibara, R. Settai, Y. Onuki, M. Hiragi, M. Ichioka, and K. Machida, *Phys. Rev. Lett.* **104**, 037002 (2010).
- [26] A. Akbari and P. Thalmeier, *Phys. Rev. B* **86**, 134516 (2012).
- [27] Y.-F. Yang, D. Pines, and N. J. Curro, *Phys. Rev. B* **92**, 195131 (2015).
- [28] Y.-F. Yang and Y. Li, *Acta Phys. Sin.* **64**, 217401 (2015).
- [29] K. Haule, C.-H. Yee, and K. Kim, *Phys. Rev. B* **81**, 195107 (2010).
- [30] H.-T. Ma, X. Ming, X.-J. Zheng, J.-F. Wen, Y.-C. Wang, Y. Liu, and H. Li, *Phys. Rev. B* **107**, 075124 (2023).
- [31] X.-G. Zhu, Y. Liu, Y.-W. Zhao, Y.-C. Wang, Y. Zhang, C. Lu, Y. Duan, D.-H. Xie, W. Feng, D. Jian *et al.*, *npj Quantum Mater.* **5**, 47 (2020).
- [32] T.-S. Nam, C.-J. Kang, D.-C. Ryu, J. Kim, H. Kim, K. Kim, and B. I. Min, *Phys. Rev. B* **99**, 125115 (2019).
- [33] H. Lu and L. Huang, *Phys. Rev. B* **94**, 075132 (2016).
- [34] T.-S. Nam, J. Kim, C.-J. Kang, K. Kim, and B. I. Min, *Phys. Rev. B* **103**, 045101 (2021).
- [35] K. Cheng, X. He, H. Yang, B. Zhou, Y. Li, and Y. Luo, *Phys. Rev. B* **100**, 205121 (2019).
- [36] U. Pfannenschmidt, F. Behrends, H. Lincke, M. Eul, K. Sch afer, H. Eckert, and R. P ottgen, *Dalton Trans.* **41**, 14188 (2012).
- [37] S. Paschen and Q. Si, *Nat. Rev. Phys.* **3**, 9 (2021).
- [38] E. M. Nica, S. Ran, L. Jiao, and Q. Si, *Front. Electron. Mater.* **2**, 944873 (2022).
- [39] B. G. Jang, B. Goh, J. Kim, J. N. Kim, H. Kang, K. Haule, G. Kotliar, H. Choi, and J. H. Shim, *Phys. Rev. B* **105**, 115147 (2022).
- [40] Q. Si and F. Steglich, *Science* **329**, 1161 (2010).
- [41] S. Doniach, *Physica B+C* **91**, 231 (1977).
- [42] A. L. Cornelius, A. J. Arko, J. L. Sarrao, M. F. Hundley, and Z. Fisk, *Phys. Rev. B* **62**, 14181 (2000).
- [43] A. Koitzsch, S. V. Borisenko, D. Inosov, J. Geck, V. B. Zabolotnyy, H. Shiozawa, M. Knupfer, J. Fink, B. B uchner, E. D. Bauer, J. L. Sarrao, and R. Follath, *Phys. Rev. B* **77**, 155128 (2008).
- [44] B. B. Zhou, S. Misra, E. H. da Silva Neto, P. Aynajian, R. E. Baumbach, J. D. Thompson, E. D. Bauer, and A. Yazdani, *Nat. Phys.* **9**, 474 (2013).
- [45] M. P. Allan, F. Masee, D. K. Morr, J. Van Dyke, A. W. Rost, A. P. Mackenzie, C. Petrovic, and J. C. Davis, *Nat. Phys.* **9**, 468 (2013).
- [46] Y. Liu, H. Li, G.-M. Zhang, and L. Yu, *Phys. Rev. B* **86**, 024526 (2012).
- [47] Y.-F. Yang, G.-M. Zhang, and F.-C. Zhang, *Phys. Rev. B* **108**, L201108 (2023).
- [48] H. Li, Y. Liu, G.-M. Zhang, and L. Yu, *J. Phys.: Condens. Matter* **27**, 425601 (2015).
- [49] Q. Y. Chen, D. F. Xu, X. H. Niu, J. Jiang, R. Peng, H. C. Xu, C. H. P. Wen, Z. F. Ding, K. Huang, L. Shu, Y. J. Zhang, H. Lee, V. N. Strocov, M. Shi, F. Bisti, T. Schmitt, Y. B. Huang, P. Dudin, X. C. Lai, S. Kirchner *et al.*, *Phys. Rev. B* **96**, 045107 (2017).
- [50] Q. Y. Chen, D. F. Xu, X. H. Niu, R. Peng, H. C. Xu, C. H. P. Wen, X. Liu, L. Shu, S. Y. Tan, X. C. Lai, Y. J. Zhang, H. Lee, V. N. Strocov, F. Bisti, P. Dudin, J.-X. Zhu, H. Q. Yuan, S. Kirchner, and D. L. Feng, *Phys. Rev. Lett.* **120**, 066403 (2018).
- [51] M. Vekic, J. W. Cannon, D. J. Scalapino, R. T. Scalettar, and R. L. Sugar, *Phys. Rev. Lett.* **74**, 2367 (1995).
- [52] F. F. Assaad, *Phys. Rev. Lett.* **83**, 796 (1999).
- [53] H. Li, H.-F. Song, and Y. Liu, *Europhys. Lett.* **116**, 37005 (2016).
- [54] A. O. Fumega and J. L. Lado, *arXiv:2401.10855*.
- [55] H. Ikeda, M.-T. Suzuki, and R. Arita, *Phys. Rev. Lett.* **114**, 147003 (2015).
- [56] G. Pang, M. Smidman, J. Zhang, L. Jiao, Z. Weng, E. M. Nica, Y. Chen, W. Jiang, Y. Zhang, W. Xie, H. S. Jeevan, H. Lee, P. Gegenwart, F. Steglich, Q. Si, and H. Yuan, *Proc. Natl. Acad. Sci. USA* **115**, 5343 (2018).
- [57] E. Bauer, G. Hilscher, H. Michor, Ch. Paul, E. W. Scheidt, A. Gribanov, Yu. Seropegin, H. No el, M. Sigrist, and P. Rogl, *Phys. Rev. Lett.* **92**, 027003 (2004).

- [58] L. V. Pourovskii, P. Hansmann, M. Ferrero, and A. Georges, *Phys. Rev. Lett.* **112**, 106407 (2014).
- [59] P. Gegenwart, Q. Si, and F. Steglich, *Nat. Phys.* **4**, 186 (2008).
- [60] Y. Aoki, T. Tayama, T. Sakakibara, K. Kuwahara, K. Iwasa, M. Kohgi, W. Higemoto, D. E. MacLaughlin, H. Sugawara, and H. Sato, *J. Phys. Soc. Jpn.* **76**, 051006 (2007).
- [61] E. Slooten, T. Naka, A. Gasparini, Y. K. Huang, and A. de Visser, *Phys. Rev. Lett.* **103**, 097003 (2009).
- [62] A. Huxley, E. Ressouche, B. Grenier, D. Aoki, J. Flouquet, and C. Pfleiderer, *J. Phys.: Condens. Matter* **15**, S1945 (2003).